Master Thesis in Experimental Nuclear Physics

Characterization of the MAPD3-N Multipixel Avalanche Photodiode

by

Per-Ivar Lønne

Department of Physics and Technology

University of Bergen

August 2010

Contents

List of Figures

Acknowledgements

First of all I want to thank my supervisor, Professor Dieter Röhrich, for giving me the opportunity to work with a very interesting topic for my master thesis. Thank you for the the help received during the work with the thesis, for clarifying discussions and suggestions for improvement.

I would also like to thank Njål Brekke who has helped me understand the experimental setup, and helped me with troubleshooting countless times. I also greatly appreciate the discussions with Hege A. Erdal, Dominik Fehlker, Andreas T. Samnøy and Lars Husdal. Thanks to Roald Langøen from the mechanical workshop at the Department of Physics and Technology for his patience and assistance in creating various parts for the experiment. I would also like to thank Fedor Guber and Alexander Ivashkin at the PSD experiment at NA61 at CERN.

Finally I would like to thank my family who has always supported me and encouraged me to study, and a great thanks also goes out to all the friends who have made the time as a student in Bergen as fun as it has been.

Summary

The objective of this thesis has been to characterize Multi-pixel Geiger-mode Avalanche Photodiodes (G-APDs), or more specifically the MAPD3-N from Zecotek Photonics, with the focus on the determination of the quantum efficiency. The Subatomic group at the Department of Physics and Technology at the University of Bergen has a long experience in the field of calorimetry. Recent developments of the G-APD detectors have increased the interest for using these detectors in various experiments, e.g. the Projectile Spectator Detector (PSD), a hadronic calorimeter located at NA61/SHINE, CERN. Obtaining a detailed knowledge of the characteristics of the G-APDs has thus become an interesting new topic at the detector lab at the department, and several projects have been started there in order to characterize and test these devices.

Previously Hege A. Erdal has characterized two different types of G-APDs [1], and Andreas T. Samnøy [2] performed a study of the uniformity of the pixel response of two types of Hamamatsu MPPC G-APDs.

This thesis builds on the work Hege performed in her master thesis, using the same experimental setup as a basis. The main objectives have been to improve the setup, adjusting it to the requirements of the MAPD3-N, and installing a system for determining the spectral response of the device. Due to the gain of the MAPD3-N, being of an order of 10-100 times lower than that of the previously characterized G-APDs, special consideration has been taken in order to improve the signal-to-noise ratio. In addition, the changes to the setup have been made in order to stabilize the components of the setup, making a more rigid system with an improved repeatability of measurements.

The main goals of the thesis has been to improve the signal to noise ratio of the MAPD readout in order to observe distinct peaks for single photons. Being able to distinguish these peaks allow the determination of the absolute gain of the detector. This has previously not been accomplished at the detector lab for the MAPD3s, and accomplishing to obtain these characteristics would be an important upgrade for the experimental setup, allowing it to determine the properties for a wider range of detectors, and to improve the resolution for those measurements that could already be determined with the original setup. In order to determine the optimal operational bias voltage applied to each specific MAPD3-N sample, it is desired to measure the dark current. By studying how the dark current and the gain varies with the bias voltage, the optimal bias voltage can be set to a level where the gain is as high as possible, without causing the dark current to increase substantially. A high gain-to-dark current ratio is important in order to ensure an optimized performance of the detector. The main goal, and the most significant change to the system, is the implementation of a monochromator. This allows a selection of the wavelength of light sent towards the detector, and in this way the spectral response to be studied. Knowing the quantum efficiency of the detector for various wavelengths will make it possible to match the wavelength of the light being detected to the spectral response of the detector, and thus improving its resolution.

The first chapter of the thesis will establish the theory of interactions between particles with matter. A detailed knowledge of the interactions can serve as a basis for a detector system, making it possible to detect particles and determine their properties. The second chapter discusses photon detectors, and introduces the concepts of scintillators, semiconductor detectors, with an emphasis on semiconductors used for photon detection, and then discusses different types of detectors, such as the PIN diode with no intrinsic amplification, onwards to Avalanche Photodiodes and more advanced Multipixel Geiger-mode APDs. Chapter 3 briefly mentions how the MAPD can be utilized in a hadronic calorimeter, which is being done for the PSD detector at NA61/SHINE, CERN. Chapter 4 gives a more detailed description of the properties of the MAPD3-N, and goes through the components of the experimental setup for the characterization of the detector. Various improvements of the signal-to-noise ratio will be discussed, and the resulting possibility and limitations of new measurements for the MAPD3-N will then follow, before moving on to the results (Chapter 5). The last chapter contains a short conclusion of the thesis, and also makes suggestions for future upgrades and improvements for the experimental setup, which could lead to an even better characterization of multipixel Geiger-mode APDs.

Chapter 1

Interactions of particles with matter

In detector physics, the aim is to determine the properties of the particles traveling through a detector. In order to determine these properties, be it the energy, mass, particle type, charge, it is important to understand how the particle interacts with matter. Numerous types of interactions may occur, determined by the properties of the particle and those of the material it passes through. Charged particles may participate in interactions that neutral particles, such as photons, will ignore and vice versa. Various processes might also be more important at certain ranges of energy, others only happen under specific conditions. If the various interactions between particles and matter are understood, the knowledge of these processes can be used to determine properties about the particles, and in that way form the basis for a detector. This section will focus on some of the general processes of interaction that should be kept in mind while working with calorimeters and semiconductor detectors, such as the *Multi-pixel Avalanche Photodiode* (MAPD). A more specific description of how semiconductors themselves function will follow in Section 2.2.

1.1 Energy loss of heavy charged particles

Heavy[1] charged particles traveling through a material will mainly either collide inelastically with the atomic electrons of the material, or scatter elastically from nuclei in the material. Inelastic collisions will cause a loss in energy of the incident particle and ionize the atom. Elastic scattering will, as the name implies, change the direction of the incident particle by scattering it. The major cause of energy loss of heavy particles in matter is inelastic collisions. In a single collision the maximum transferable kinetic energy to an electron depends on the mass, m_0

[1] Particles heavier than the electron, such as muons, pions, protons and alpha particles are considered to be heavy particles in this section. Heavy ions will not be discussed as a part of the heavy particles in this section.

and the momentum, $p = \gamma m_0 \beta c$, of the incident particle, where γ is the Lorentz factor, $\gamma = E/m_0c^2$, $\beta c = v$ and m_0 is the rest mass of the incident particle. The maximum energy that can be transferred to an electron with mass m_e is then given by [3, 4]:

$$E_{kin}^{max} = \frac{2m_e c^2 \beta^2 \gamma^2}{1 + 2\gamma m_e/m_0 + (m_e/m_0)^2} = \frac{2m_e p^2}{m_0^2 + m_e^2 + 2m_e E/c^2}. \qquad (1.1)$$

The particle will lose very little energy in each collision, but in a normally dense material the particle will collide many times per unit path length leading to a substantial total loss of energy. This is an statistical process and the average energy loss per unit length, or *stopping power*, dE/dx, can be described by the Bethe Bloch formula [5]:

$$-\frac{dE}{dx} = 2\pi N_A r_e^2 m_e c^2 \rho \frac{Z}{A} \frac{z^2}{\beta^2} \left[ln(\frac{2m_e \gamma^2 v^2 W_{max}}{I^2}) - 2\beta^2 - \delta - 2\frac{C}{Z} \right], \qquad (1.2)$$

where the variables are as follows:

- N_A: Avrogado's number
- r_e: classical electron radius $r_e = \frac{1}{4\pi\epsilon_0} \cdot \frac{e^2}{m_e c^2}$
- ϵ_0: the permittivity of vacuum
- m_e: electron mass
- ρ: density of absorbing material
- Z: atomic number of absorbing material
- A: Atomic weight of absorbing material
- C: shell correction
- z:charge of incident particle (in units of e)
- $\beta = \frac{v}{c}$ of incident particle
- $\gamma = \frac{1}{sqrt1-\beta^2}$
- W_{max}: maximum energy transfer in a single collision
- I: mean excitation potential
- δ: density correction

1.2 Energy Loss of Electrons and Positrons

The electron and its antiparticle, the positron, can lose energy due to collisions in a similar way as the heavy charged particles. There are, however, some differences that make the energy of these light particles differ from the energy loss of heavier particles, namely their low mass, and the fact that an incident electron can not be distinguished from the target electrons in a collision. Due to the light mass, these particles can not be assumed to remain undeflected during a collision process. As the particles have a very small mass, they are also subject to an additional effect called *bremsstrahlung*, which is the emission of electromagnetic radiation due to the acceleration or deceleration of a charged particle, e.g. when an electron is scattered from the electric field of an atom. At energies above a few 10's of MeV, the energy loss by radiation is comparable to the collision-ionization loss, and at

even higher energies bremsstrahlung is the main contributor to the energy loss [5]. There are also possibilities for mechanisms such as Bhabha and Møller scattering, positron annihilation etc. Combining the factors leads to an equation for the total energy loss of electrons and positrons consisting of two parts, one for the radiation loss and one for collision losses:

$$(\frac{dE}{dx})_{tot} = (\frac{dE}{dx})_{rad} + (\frac{dE}{dx})_{coll}. \tag{1.3}$$

The energy where the energy loss due to radiation and the energy loss due to collisions are equal is referred to as the critical point, or the critical energy.

1.2.1 Energy loss due to radiation

When a fast, charged particle interacts with the Coulomb field of a nucleus, it will be decelerated and a fraction of its kinetic energy is emitted as photons. This process is known as *bremsstrahlung* and is responsible for the main loss of energy for electrons and positrons at energies above the critical energy. The energy loss by bremsstrahlung for high energies can be described as [3, 4]:

$$-\frac{dE}{dx} \approx 4\alpha N_a \cdot \frac{Z^2}{A} z^2 r_e^2 \cdot E \cdot ln\frac{183}{Z^{1/3}}, \tag{1.4}$$

where z, m and E are the charge number, mass and energy of the incident particle. The energy loss of electrons from bremsstrahlung can be given as [3]:

$$-\frac{dE}{dx} \approx 4\alpha N_a \cdot \frac{Z^2}{A} r_e^2 \cdot E \cdot ln\frac{183}{Z^{1/3}}, \tag{1.5}$$

if $E >> m_e c^2/\alpha Z^{1/3}$. When considering electrons we set $z = 1$, $m = m_e$ and equations 1.4 and 1.5 can be written as:

$$-(\frac{dE}{dx})_{rad} = \frac{E}{X_0}. \tag{1.6}$$

X_0 is the *radiation length*, which is defined as the distance over which the electron energy is reduced by a factor 1/e due to radiation loss only [5]. For a charged particle that traverses matter and is subject to multiple Coulomb scattering, the radiation length can be given as [3, 4, 6]:

$$X_0 = \frac{A}{4\alpha N_A Z^2 r_e^2 ln(183 Z^{-1/3})}. \tag{1.7}$$

From this equation the proportionality $X_0^{-1} \propto Z^2$ is obtained, describing the interactions of the incident electron with the Coulomb field of the target. In addition to interactions with the field of nuclei, the incident electrons are also subject to bremsstrahlung while interacting with electrons orbiting the target nuclei. The additional charge due to orbiting electrons is proportional to the number of target electrons (equal to the atomic number, Z, for an atom of neutral charge). By replacing the term Z^2 with $Z(Z+1)$ in Equation 1.7 the additional

factor is included. After taking the screening effects of the nucleus from the electrons into account, the radiation length can finally be approximated by [3,7–9]:

$$X_0 = \frac{716.4 \cdot A[g/mol]}{Z(Z+1)ln(287/\sqrt{Z})} g/cm^2. \tag{1.8}$$

1.2.2 Energy loss due to collisions

The Bethe-Bloch formula presented in 1.2 can also be used for electrons and positrons if a few changes are made. For the heavy charged particles, the incident particle is assumed to remain undeflected during the collision process, but this assumption is not valid for the electrons and positrons due to their low mass. In addition the electrons collide with identical electrons, making it impossible to distinguish the interacting particles from each other. These two details lead to changes in some of the terms of the Bethe-Bloch formula [5]:

$$-\frac{dE}{dx} = 2\pi N_a r_e^2 m_e c^2 \rho \frac{Z}{A} \frac{1}{\beta^2} \left[ln \frac{\tau^2(\tau+2)}{2(I/m_e c^2)^2} + F(\tau) - \delta - 2\frac{C}{Z} \right], \tag{1.9}$$

where τ is the kinetic energy of the particle in units of $m_e c^2$. The function $F(\tau)$ is different depending if the incident particle is an electron or a positron.

1.3 Photon interactions

Photons are neutral particles and are usually detected indirectly as the photons produce charged particles in an interaction, which in turn can be observed through their ionisation in the sensitive volume of the detector. When photons travel through matter, they can interact with the material in various ways, and the outcome of such interactions can either be a complete absorption of the photon or scattering of it. To describe the attenuation of electromagnetic waves, or photons, traversing matter, one can look at the ideal case of monoenergetic, homogenous radiation. The intensity, I, of the photonbeam will decrease exponentially with respect to the thickness of the absorption material. If the incident intensity is named I_0, the intensity after the beam has passed a thickness of x of the absorbing material will be [10]:

$$I = I_0 e^{-\mu x} \Rightarrow \frac{dI}{dx} = -\mu I_0 e^{-\mu x} = -\mu I. \tag{1.10}$$

μ is called the linear attenuation coefficient and is given in the unit of m^{-1}. This coefficient gives a measure of how much of the beam is scattered or absorbed per unit length in a material and is defined as:

$$\mu = \frac{\sigma_{tot} N_A}{A}, \tag{1.11}$$

where N_A is Avogadros number and A is the molecular weight. The total cross section, σ_{tot}, represents all the processes participating in the attenuation of a

photon beam. The attenuation of photons depends on the energy of the photons. The main causes of attenuation are the photoelectric effect, Compton scattering and pair production. While the two former effects are of lesser importance at higher energies (above a few MeV, the probability for pair production interactions to take place increases). These three processes will be discussed in the following sections. There are also a few other processes of lesser importance in this energy range, such as Rayleigh scattering, Thomson scattering and the photonuclear effects, but these will not be discussed in this thesis. The different processes will have a varied cross section at different energies, and a figure of such energy dependencies can be seen in Figure 1.1.

1.3.1 The Photoelectric effect

The photoelectric effect is a process in which the incident photon is absorbed by an atomic electron, primarily an inner shell electron (K-shell), releasing the electron from the atom as seen in Figure 1.2. In order for this to take place, the energy of the photon needs to exceed the binding energy of the electron. The ejected electron will then have the energy of the incident photon minus the binding energy of the electron, E_b and the recoil energy of the atom, E_A, $E_K = h\nu - E_b - E_A \approx h\nu - E_b$. The latter approximation is acceptable due to the relation $E_K/E_A \approx m/M < 1/1840$[2], where m is the electron mass and M is the mass of the atom. For an electron to participate in the photoelectric effect it has to be bound to an atom so that the nucleus can absorb the recoil energy. The cross section for the photoelectric effect decreases with increasing photon energies, but will increase as the energy reaches the binding energy of a new electron shell of an atom, such that those electrons are made available for ionization. Finding a simple analytical expression for the cross section of the photoelectric effect is complicated, but by limiting the cross section to the K-shell and assuming that we can calculate the expression non-relativistic, allows us to use the Born approximation, yielding [10]:

$$\sigma_{p.e.} = \frac{32\sqrt{2}\pi}{3}\alpha^4 r_e^2 Z^5 \left(\frac{m_e c^2}{h\nu}\right)^{7/2} \propto \frac{Z^5}{(h\nu)^{7/2}}, \tag{1.12}$$

where $\alpha = \frac{1}{137}$, $r_e = \frac{e^2}{4\pi\epsilon m_e c^2}$ and Z is the atomic number. From the equation it can be seen that the cross section increases as a function of Z^5.

1.3.2 Compton Scattering

A free[3] electron can not absorb a photon by the photoelectric effect, but it can still scatter the photons into other directions than that of the incident beam. Compton scattering is inelastic scattering of a photon by a free electron. In order to determine the energy transferred to the electron from the photon, the

[2] The relation between the mass of a proton or neutron and an electron is approximately 1/1840, so for an atom with several nucleons this term will decrease further.

[3] "A *loosely bound electron* is an electron whose binding energy E_B is small in comparison with the photon energy $h\nu$, i.e., $E_B << h\nu$. An interaction between a photon and a loosely bound electron is considered to be an interaction between a photon and a free (unbound) electron." [11]

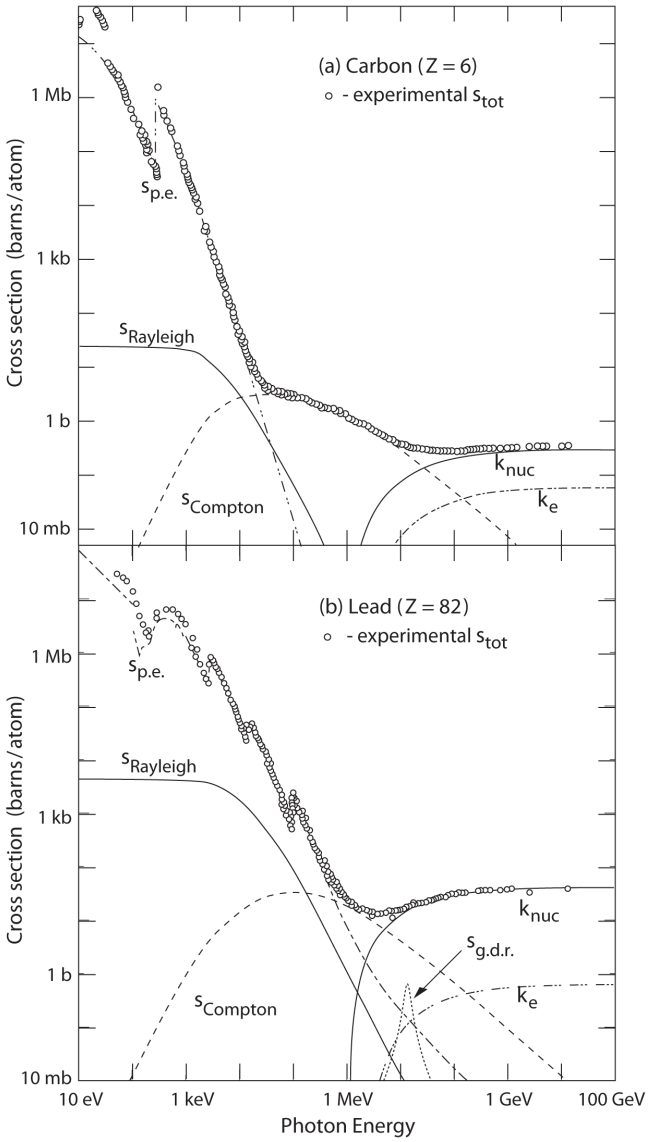

Figure 1.1: Figure from http://pdg.lbl.gov. Photon total cross sections as a function of energy in carbon and lead, showing the contributions of different processes. The cross sections are for:
$\sigma_{p.e.}$ - Photoelectric effect,
$\sigma_{Rayleigh}$ - Rayleigh (coherent) scattering,
$\sigma_{Compton}$ - Compton scattering,
κ_{nuc} - Pair production, nuclear field,
κ_e - Pair production, electron field,
$\sigma_{g.d.r.}$ - Photonuclear interactions.

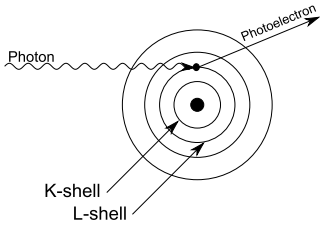

Figure 1.2: The photoelectric effect, where an incident photon kicks out an electron, preferably from one of the inner atomic electron shells, i.e. the K- or L-shell.

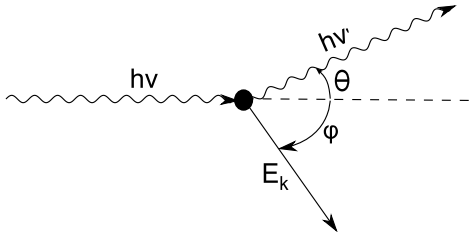

Figure 1.3: A photon is inelastically scattered off a free electron, resulting in the photon changing direction and the electron gaining kinetic energy.

Compton wavelength shift relationship (1.13) is derived, using the conservation of total energy and momentum laws:

$$\Delta\lambda = \lambda' - \lambda = \lambda_C(1 - cos\theta). \tag{1.13}$$

λ : wavelength of incident photon,
λ' : wavelength of scattered photon,
λ_C : The Compton wavelength, defined as $\lambda_C = \frac{h}{m_e c} = 0.00243$ nm.
Equation 1.13 leads to relationships for the energy of the scattered photon $h\nu$ and the energy of the recoil electron E_K as a function of the incident photon energy $h\nu$ and its scattering angle θ [11]:

$$\Delta\lambda = \lambda' - \lambda = \frac{c}{\nu'} - \frac{c}{\nu} = \frac{h}{m_e c^2}(1 - cos\theta) \text{ or,} \tag{1.14}$$

$$\frac{1}{h\nu'} - \frac{1}{h\nu} = \frac{1}{m_e c^2}(1 - cos\theta). \tag{1.15}$$

From (1.15) the following expressions for $h\nu'$ and E_K can be found:

$$h\nu' = h\nu \frac{1}{1 + \epsilon(1 - cos\theta)}, \tag{1.16}$$

$$E_K = h\nu \frac{\epsilon(1 - cos\theta)}{1 + \epsilon(1 - cos\theta)}, \tag{1.17}$$

where $\epsilon = h\nu/m_e c^2$ represents the incident photon energy $h\nu$ normalized to the electron rest energy $m_e c^2$ [11]. The maximum recoil energy possible for a Compton

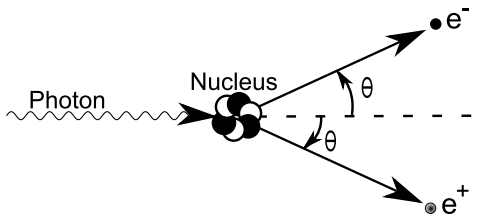

Figure 1.4: A high energy photon converts its energy to an electron-positron pair in the vicinity of a nucleus.

scattered electron is given at a scattering angle of 180°. Inserting this into 1.17 yields:

$$E_{K_{max}} = h\nu \frac{\epsilon}{1+2\epsilon}. \tag{1.18}$$

The total cross section for Compton scattering per electron, obtained by using the Klein-Nishina formula, can be written as [3]:

$$\sigma_c^e = 2\pi r_e^2 \left[\left(\frac{1+\epsilon}{\epsilon^2} \right) \left\{ \frac{2(1+\epsilon)}{1+e\epsilon} - \frac{1}{\epsilon} ln(1+e\epsilon) \right\} + \frac{1}{2\epsilon} ln(1+e\epsilon) - \frac{1+3\epsilon}{(1+2\epsilon)^2} \right] \{cm^2/electron\}, \tag{1.19}$$

where $\epsilon = \frac{E_\gamma}{m_e c^2}$, E_γ is the energy of the incident photon.

1.3.3 Pair Production

Pair production is a process where a photon is transformed into an electron-positron pair. This process can only occur for photons with energies above 1.022 MeV, since the rest energy of both the electron and positron is 511 keV each. The pair production can only take place in the vicinity of a third object, such as a nucleus or an orbital electron, in order to conserve momentum. The theoretical derivation of the atomic cross section for pair production, σ_{pp}, is very complicated, but in general the cross section in the field of a nucleus or orbital electron appear as follows [11]:

$$\sigma_{pp} = \alpha r_e^2 Z^2 P(\epsilon, Z), \tag{1.20}$$

where:

- α: is the fine structure constant $\alpha = 1/137$,
- r_e: is the classical electron radius,
- Z: is the atomic number of the absorber,
- P(ϵ, Z): is a function of the photon energy $h\nu$ and atomic number Z of the absorber, as given in Table 1.1.

Table 1.1: Characteristics of the atomic cross section for pair production in the field of the nucleus or in the field of an orbital electron [11].

Field	Energy range	P(ϵ,Z)	Comment
nucleus	$1 \ll \epsilon \ll 1(\alpha Z^{1/3})$	$\frac{28}{9} ln 2\epsilon - \frac{218}{27}$	no screening
nucleus	$\epsilon \gg 1/(\alpha Z^{1/3})$	$\frac{28}{9} ln \frac{183}{Z^{1/3}} - \frac{2}{27}$	*complete screening*
nucleus	*outside the limits above but* $\epsilon > 4$	$\frac{28}{9} ln 2\epsilon - \frac{218}{27} - 1.027$	no screening
electron	$\epsilon > 4$	$\frac{1}{Z}\left(\frac{28}{9} ln 2\epsilon - 11.3\right)$	no screening

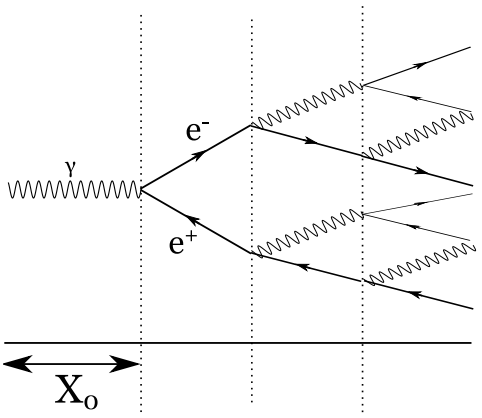

Figure 1.5: An illustration of an electromagnetic cascade, starting by a high energetic photon. Such showers can also start by an incident electron with high energy. Figure from [1].

It can be seen from Equation 1.20 and Table 1.1 that the cross section is proportional to Z^2. The table also shows that in order for pair production to take place near an orbital electron, the energy of the incident photon need to be at least $4m_e c^2 = 2.044\ MeV$. This process is often referred to as *triplet production*, as the electron which absorbs the recoil will also leave the interaction site due to the recoil energy.

1.3.4 Electromagnetic showers

As mentioned in the previous sections, there exist both processes that create photons from charged particles (e^+ and e^-) at high energies, and processes that can create charged particles from high energy photons. If a high energy photon, or charged particle, passes through matter these processes can happen several times after each other, resulting in a cascade of photons, electrons and positrons.

The shower will increase in size until the energy of the electrons and positrons drops below the critical energy. At this point, ionization processes such as atomic collisions take over the role as the dominant cause for loss of energy for the charged particles and eventually cause the particles to be stopped in the material. An illustration of an electromagnetic shower can be seen in Figure 1.5.

A simplified model [5] of an electron-photon shower can be described by imagining a high energy photon with energy E_0 entering a material. After one radiation length, X_0, the photon should statistically be subject to pair production and result in an electron-positron pair, each with energy $E_0/2$. After another radiation length these two new particles will be subject to bremsstrahlung and emit a photon with approximately half the energy of the charged particle. As a result there will now be two photons and two charged particles (e^+ *and* e^-), each with the energy $E_0/4$. As the process keep multiplying the number of particles, it can be seen that after t radiation lengths the total number of particles (e.g. electrons, positrons and photons) will be:

$$N \approxeq 2^t, \tag{1.21}$$

each with an average energy of:

$$E(t) \approxeq \frac{E_0}{2^t}. \tag{1.22}$$

The range of a shower following this model would then be:

$$E(t_{max}) = \frac{E_0}{2^{t_{max}}} = E_c, \tag{1.23}$$

if the shower is assumed to end exactly where the energy reaches E_c, the critical energy. The maximum number of particles would then be:

$$N_{max} \approxeq \frac{E_0}{E_c}. \tag{1.24}$$

This model is however only able to provide an estimation of the process, and Monte Carlo simulations are often used in order to get a more precise model. These simulations take the possibly large fluctuations of the bremsstrahlung and other statistical effects into consideration, providing a better model for electromagnetic showers.

1.3.5 Hadronic showers

A hadronic shower is a process that, similarly to the electromagnetic showers, produces a large amount of particles from an incident particle. In contrast to the electromagnetic showers, the hadronic showers are induced, as the name indicates, by high energy hadrons. A detailed understanding of hadronic cascades are complicated, due to the complexity and variety of the hadronic processes, but a brief introduction will be given here.

When a hadron with a high kinetic energy (above $\sim 5\ GeV$) enters a medium, it will interact with the medium by inelastical scattering. In this process, secondary

hadrons are produced, such as pions and nucleons. These hadrons will in turn scatter inelastically and produce more hadrons, producing a cascade of hadrons. An important parameter in the determination of the depth of a hadronic cascade within a material is the absorption length λ, given by [12]:

$$\lambda = \frac{A}{\sigma_i N_A \rho}, \tag{1.25}$$

where A is the mass of one mole of the material,N_A is Avogadros number, ρ is the density of the material and σ_i is the cross section for inelastic scattering. The transverse distribution of a hadronic shower depends on the longitudinal depth, and widens as the shower progresses through the material. Such a shower will normally consist of a high energetic core, with an outer layer of particles with lower energy that extends away from the center of the shower. The intrinsic hadronic energy resolution has been indicated, by experimental data, to be:

$$\left(\frac{\sigma_E}{E}\right)_{intrinsic} \approxeq \frac{0.45}{\sqrt{E[GeV]}}. \tag{1.26}$$

This resolution has been found to be valid for materials from Al to Pb, with the exception of ^{238}U.

Chapter 2

Photon Detection

The previous chapter discussed the interactions of particles with matter. With these interactions and properties established, this chapter will look into some detectors based upon these principles. The main focus will be the detection of photons and charged particles, and when charged particles are discussed the detection of these will mainly be indirectly through *scintillators*, which are materials that can convert the energy of incident particles into emitted light. A scintillating material is a material that will cause an emission of a flash of light, i.e. a scintillation, when hit by particles. If such a material is combined with a light detecting device, such as a *photomultiplier tube* (PMT) or a *multipixel avalanche photodiode* (MAPD), the scintillations can be read out as electrical pulses. These pulses can be analyzed to provide information about the incident particle or radiation.

2.1 Scintillators

Ionizing radiation which interacts with a material will excite the atoms or molecules of the material or excite electron-hole pairs in crystals, which will emit photons as they deexcite again. The wavelength of the photon depends on the material and for some materials lies in or near the electromagnetic spectrum of visible light. This phenomenon is called *radioluminescence* or *scintillation* and has proven to be useful for particle detection. In a scintillator meant for radiation detection there are certain properties which the scintillator should possess [13]:

- The material should be transparent to the wavelength of the emitted scintillation light.
- The efficiency of light production should be large, i.e. a high amount of the excitation energy should be converted into light.
- The light pulses should be as short as possible and there should be little or no delayed light emission.

- The amount of light emitted should be proportional to the energy deposited by the ionising particle.
- The refractive index of the material should be close to 1.5 (the recractive index of air) so that light can easily be extracted from the scintillator.
- The material should be chemically and mechanically stable and not too difficult or expensive to produce.

There are in general two groups of scintillators, namely organic and inorganic. Organic scintillators contain mainly atoms with a small atomic charge, Z, resulting in a long radiation length, X_0. Inorganic scintillators contain a large fraction of heavy atoms resulting in a short radiation length. Due to this difference the two types of scintillators are used for different purposes. Organic scintillators are used for charged particle tracking and detection of fast neutrons (in the energy range of $\approx$ 10keV - 10MeV), while inorganic scintillators are used in electromagnetic calorimeters, to detect photons, electrons and positrons.

2.1.1 Organic Scintillators

Organic scintillators come in three types: Organic crystals, organic liquids or plastic scintillators. The scintillation light emitted from these scintillators originates from transitions made by the free valence electrons of the molecules.

Organic crystals

The organic crystals are very effective scintillators but are rarely used any longer due to being expensive and difficult to use, compared to plastic scintillators.

Organic liquid scintillators

Organic liquid scintillators are organic scintillators dissolved in an appropriate solvent. Wavelength shifters are often added in order to improve the transparency of the scintillator and to better match the spectral sensitivity of the detection device. Organic liquid scintillators are less expensive to produce than other scintillators and are therefore often used when large volumes are nessecary. Another useful field of application is to count the radiation from a material that can easily be dissolved in the liquid, and is often used for ^{14}C dating of archaeological samples [13].

Plastic scintillators

Plastic scintillators are the most widely used class of organic scintillators in nuclear and particle physics. These scintillators are solutions of organic scintillators, but unlike the liquid scintillators they are dissolved in a solid plastic solvent. The light emitted from the plastic scintillators are normally in the UV spectrum and only have a mean free path of a few millimeters. A wavelength shifter is therefore needed in order to absorb the light and re-emit it at a longer wavelength, which has

a much longer mean free path, allowing the light to travel further. The wavelenght shifters absorbation spectrum should match the emission spectrum of the primary emitter, i.e. the pure plastic scintillator, and its emission spectrum should match the spectral range of the detector that yields the highest efficiency of detection. If this is not the case, a second wavelength shifter can be added, which provides a better match towards the detector. A great benefit by using plastic scintillators is that they are easily produced and can be shaped into a wide variety of forms, ranging from large, thin sheets to blocks or even fibers. The plastic scintillators also have a short decay time, about 2-3 ns [5], and can therefore provide a good timing resolution. In addition, they also have a high light output. The combination of these properties makes them ideal for hadronic calorimeters, as they normally require a large amount of material. The plastic scintillators are mechanically stable, but care should be taken not to let them come in contact with organic solvents such as acetone or similar products as these may damage the scintillator.

2.1.2 Inorganic Scintillators

Inorganic scintillators are usually ionic crystals. The mechanics of light emission for these scintillators rely on the energy band structure of the crystal. This process results in a slower response than for the organic scintillators, by about 2-3 orders of magnitude lower due to phosphorescence [5]. The band structure of the crystal consists of a valence band and a conduction band, separated by a band gap, known as the *forbidden energy gap*. In a simplified model for an ionic crystal the valence band should be filled by electrons and the conduction band should contain no electrons. The energy gap contains no electron energy levels, and thus cannot contain any electrons. For a material to be transparent, this band gap is required to be larger than ≈ 3 eV [13]. In order for the crystal to be able to transmit light it is dependent on *luminescence centers* with localized levels in the band gap of the crystal. Such centers may occur naturally in the material but are usually provided by adding a small amount of dopant to the material. When radiation interacts with the crystal it can excite an electron from the valence band into the conduction band. This allows electrons from deeper energy bands to fill the hole left by the excited electron and they may get further excited to the conduction band as well by the use of excess energy. The results is that one X-ray or gamma ray gets converted into several phonons, i.e. thermal energy, in the crystal [13]. In this process a large number of electron-hole pairs[1] are created. In order for the scintillator to be efficient it is important that the electrons and holes reach the luminescence centers in the band gap. The introduction of suitable dopants to the crystal should provide energy levels both close to the valence band (activator ground states) and levels close to the conduction band (activator excited states) as seen in Figure 2.3b and c. The difference between these levels will correspond to the energy of the scintillation photons emitted from the transition from the excited state to the ground state, and if a suitable dopant is chosen the transition will result in a visible photon.

[1] Energy band gap structures, electron-hole pairs and doping processes affecting the band gap structures are discussed in more detail in Section 2.2.

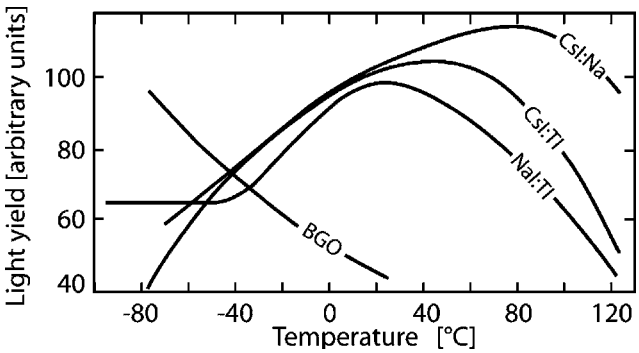

Figure 2.1: Light yield of some scintillators as a function of temperature [13, 15]

The scintillation properties of inorganic scintillators often have a strong dependence on the temperature. This dependence varies for different crystals, but for many it will first increase with increasing temperature, reach a maximum and then decrease again, as seen in Figure 2.1. An explanation to this effect is that impurities in the crystal lattice can create shallow band gap traps, which may be able to retain electrons or holes at low energies, preventing them from reaching the luminescence centers. As the temperature rises, the traps will no longer be able to retain the charges and as a result the light yield is increased. The following saturation can be explained by an effect of the activator states known as thermal quenching. The distance between these states may vary depending on the permanent thermal motion of the ions around the luminescence center. This can result in the distance between the states becoming small, allowing the electron to jump to the lower level without emitting an optical photon, but rather interacting with the phonons[2] in the lattice, yielding a non-radiative transition [13]. The probability of this process increases with increased temperatures, decreasing the light yield from the scintillator. Another problem with the inorganic scintillators is that some of them are hygroscopic, meaning that they attract water molecules from the surrounding enviroment such as the humidity of the air or moisture from the skin while handling them. The main advantage of the inorganic scintillators is the high density and high atomic number giving them a small radiation length. In addition they have a high light output which improves the energy resolution [5]. At energies below 1 MeV the energy resolution may however be limited for some inorganic scintillators if the energy response is not linear. This is caused by the fact that the energy of the radiation may be deposited in many different ways in the crystal, i.e. by depositing all of its energy in one photoelectron, or by one or more Compton interactions before losing all of its energy by the photoelectric effect. At higher energies however, this effect tend to become less important [13].

[2]A phonon is a quasi particle characterized by the quantization of the modes of lattice vibrations in a uniform solid material. The atoms are bound together by bonds, and thus they can not vibrate independently, but take form of a wave propagating through the material. The collective vibrational modes in periodic solids can only accept energy only in discrete amounts, and these quanta are referred to as phonons [14].

Table 2.1: Properties of some commonly used inorganic scintillators [13].

Name	Density	Emission λ [nm]	Light yield [photons/MeV]	Decay time τ [ns]	Radiation Length [cm]
NaI:Tl	3.67	410	40,000	230	2.59
BGO	7.14	480	4000	300	1.12
BaF_2 (fast)	4.88	215	1500	¡1	2.05
BaF_2 (slow)	4.88	310	10,000	700	2.05
CsI:Tl	4.51	565	65,000	600	1.68
CsF	4.11	390	2000	3	
$PbWO_4$	8.28	480	200	10	0.89
LSO:Ce	7.4	420	28,000	40	1.14
LuAP:Ce	8.3	360	10,000	18	
GSO:Ce	6.71	440	7500	60	1.38
$LuPO_4$	6.6	360	13,000	24	
YAP:Ce	5.37	370	16,000	25	2.7
LaBR:Ce	5.3	360	60,000	35	2.13

The characteristics of the inorganic crystals will vary highly between the individual crystal types. Some have better response times but might be more exposed to other unfortunate effects, some are more sensitive to humid enviroments than others, etc. It is therefore important to investigate which scintillator is best for a specific application. A list of some commonly used inorganic scintillators can be seen in Table 2.1.

2.2 Semiconductor Detectors

Semiconductor detectors are based on crystalline semiconductor materials, as the name implies, such as silicon and germanium. The real development of these instruments first began in the late 1950's and reached commercial availability in the 1960's. They were soon being used widely in nuclear physics research for particle detection and gamma spectroscopy. In the later years there has been a major development of such devices and improvements have made them useful in new areas such as high energy physics and also in medical diagnostics with the Positron Emission Tomography (PET) technology [5].

A semiconductor detector follows a similar basic operating principle as a gaz ionization detector, but whereas the latter uses gas as its detecting medium, the former uses a solid semiconductor material. When ionizing radiation pass through the medium an electron-hole pair is created, instead of the electron-ion pair created in the gas ionization devices. The pairs are then collected in an electric field. Foh the semiconductor detectors, a lower average energy is required to create an event than the energy required for gas ionization, leading to a higher energy resolution for the semiconductor detectors. In addition the semiconductor materials have a higher density than the gas, and hence a higher stopping power, resulting in a compact size and fast response times.

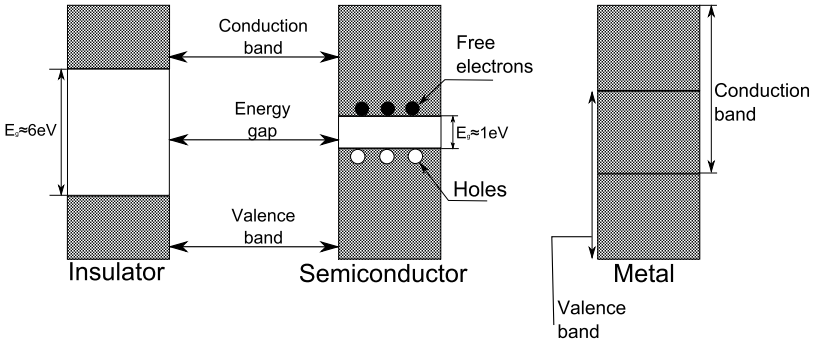

Figure 2.2: The energy band structure of an insulator, a semiconductor and a conductor/metal [5].

Having introduced the concept of semiconductors briefly, we will now take a look at how a semiconductor functions. In its simplest form, a pure (also known as intrinsic) semiconductor is considered to be without impurities. A semiconductor will in reality never be completely pure, and the impurities are important for the detectors as we will see later, but we will start out by looking at an ideal case of a pure material. The outer shell atomic levels exhibits an energy band structure consisting of:

- A valence band with tightly bound electrons which remain associated to their respective lattice bands.
- A forbidden energy gap where no energy levels are available. This band is large for insulators, smaller for semiconductors and nonexisting for conductors, as seen in Figure 2.2.
- A conducting band where electrons are detached from their parent atoms and can roam freely through the crystal.

The small gap between the valence and conducting band in a conductor makes it very easy for thermally excited electrons to enter the conducting band. For a semiconductor this effect is smaller, and only a few thermally excited electrons will jump to the conducting band. If an electric field is applied, there will still be a small current through the semiconductor. This effect decreases if the semiconductor is cooled, as more the electrons will then fall into the valence band.

2.2.1 Charge carriers in semiconductors

At 0 Kelvin there will be no thermal excitation of the electrons in the valence band of the semiconductor, and all electrons participate in covalent bonding between the lattice atoms. At higher temperatures, thermal energy can excite an electron into the conducting band, leaving a hole in its original position. These holes can be seen as a positive charge in the valence band and a nearby valence electron may easily jump to this hole to fill it, leaving a new hole in its original position.

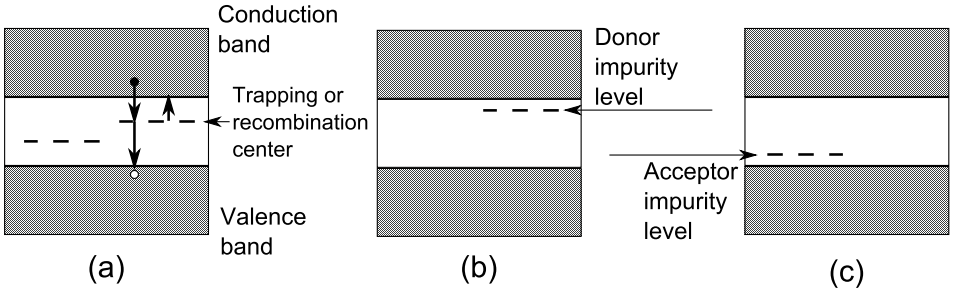

Figure 2.3: (a) Impurities in the semiconductor leads to deep trapping and recombination centers near the middle of the forbidden energy gap. (b) Shallow donor impurity levels added to the forbidden band gap of a n-type semiconductor, close to the conduction band. (c) Shallow acceptor impurity levels added to the band gap of a p-type semiconductor, close to the valence band [5].

This results in the hole appearing as a positive charge carrier moving through the crystal, contributing to the electric current. The semiconductor therefore has two contributors to the electric current, namely the holes in the valence band and the free electrons in the conducting band.

2.2.2 Recombination and trapping

An electron can recombine with a hole in various ways, with the most basic one being when an electron drops from the conducting band into an open level in the valence band resulting in the emission of a photon. This process is called *direct recombination*, and is the opposite effect of the electron-hole generation. This process require exactly correct values of energy and momentum of both the electron and the hole, making the occurence very rare.

Another mechanism that is very important is the recombination through *recombination centers*, caused by impurities in the crystal. The impurities lead to additional energy levels in the forbidden energy gap as seen in Figure 2.3a. After capturing an electron from the conducting band into an recombination center, the center can either hold the electron for a while before releasing it back into the conduction band, or capture a hole as well before the electron is released, causing the electron-hole pair to annihilate. A typical concentration for impurities should not exceed 10^{10} impurities/cm^3 for large volume detectors [5], as there needs to be a balance between the recombination frequency and the collection time of the charges in order to avoid a reduction in resolution due to charge loss.

Another effect caused by impurities in the crystal is trapping. This happens when an impurity is only capable of capturing one kind of charge carrier, i.e. either an electron or a hole. This results in the carrier being held for a period of time before being released, without the possibility of being recombined. If the trapping time is long, and particularly if it is close to the charge collection time or higher, a reduction of the resolution will occur. For short trapping times, however, the effect does not result in any noticable loss in resolution.

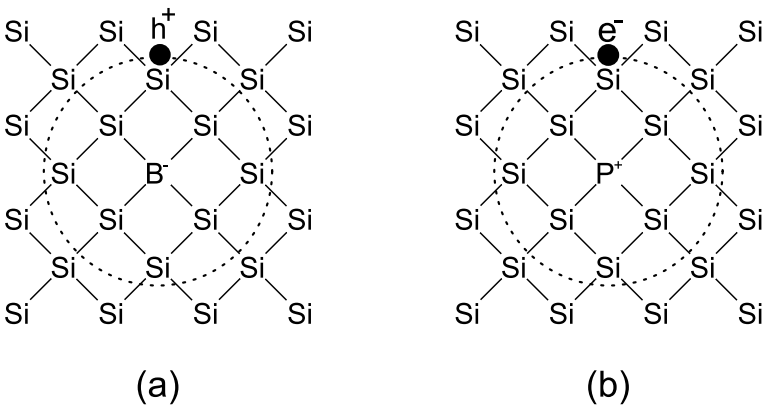

Figure 2.4: Doped silicon lattices. The lattice in (a) is doped by introducing boron atoms, resulting in an excess of holes. This is called a p-type doping. In (b) an phosphorous atom has been introduced to the lattice, resulting in an extra electron. This is called n-type doping. [16]

2.2.3 Doped Semiconductors

A pure semiconductor will have an equal amount of holes in the valence band and electrons in the conducting band. This balance can, however, be changed by adding a small amount of impurities to the crystal, in the form of atoms with one more or one less valence electron, as seen in Figure 2.4. This process is called doping the semiconductor, and depending on the type of impurity you have either a n-doping, where you add atoms with 5 valence electrons (donors), or p-doping where you add atoms with 3 valence electrons (acceptors). Two commonly used dopants are phosphorous and boron, which are n- and p-type dopants, respectively. It is also possible to use materials such as Zn and Cd (double acceptors) or S and Sn (double donors) [16].

In a n-doped crystal there will be an extra electron that does not fit into the valence band, as seen in Figure 2.4, and the presence of the impurity atoms result in a discrete energy level (Figure 2.3b and c) created in the energy gap, which the electron will occupy. This level lies extremely close to the conducting band and the electron is easily exited to the conduction band, increasing the conductivity of the semiconductor. In addition, the electrons can also fill holes created termally, causing the concentration of holes to decrease in the crystal. This results in a majority of the charge carriers being electrons [5].

The other possibility is doping the semiconductor with atoms containing 3 valence electrons. In this situation there will not be enough electrons to form all the covalent bands, causing an excess of holes in the crystal. Similarly to the n-doped crystal, there will now be created an additional state in the energy gap, but in this situation the state will be close to the valence band. Electrons in the valence band are easily excited into this new state, leaving extra holes behind. The excess of holes will also cause a decrease in the number of free electrons, resulting in holes being the main charge carriers. This is called p-type doping [5].

2.2.4 p-n Junctions

When used for detecting radiation the semiconductor is depending on a semiconductor junction, which is created by combining a p-type and a n-type semiconductor. Due to the uneven distribution of electrons and holes in the two materials, there will be an initial diffusion of holes towards the n-region and similarly a diffusion of electrons towards the p-region. These drifting charge carriers will recombine, causing an electric field gradient across the junction due to static ion charges. After a while a thermal equilibrium is reached and this process stops as the space charge potential exceeds the available energy for thermal diffusion, leaving a region of immobile space charge in the junction. This region is known as the *depletion zone* or *space charge region*, and due to the region of positive ions on the p-type side and the negative ions on the n-type side, there will be an electric field from the n-type side towards the p-type side, as seen in Figure 2.5a. This field is often referred to as the built-in electric field. The charge density will be positive on the n-type side, and negative on the p-type side of the space charge region [16]. Any electron or hole created in or entering this region will be pulled out by the electric field, making this region very useful for detecting radiation. When ionizing radiation enters the depletion region and creates an electron-hole pair, this pair will be swept out by the electric field, causing a current signal proportional to the ionization. This signal can then be read out by placing electric contacts to each side of the semiconductor [5]. In Figure 2.5b, a diagram of the electron energy levels is displayed, showing the creation of the potential between the p- and n-region. In a pure semiconductor the Fermi level[3] is in the middle of the band gap. For a doped region however, the Fermi level will be shifted towards the valence band when acceptors (p-type) are introduced, and towards the conduction band when adding donators (n-type). When regions are combined into a p-n junction and reach a thermal equilibrium, the Fermi level will be constant throughout the device [16, 18]. In order for this to be possible, the valence and conductive bands have to bend throughout the device, meaning that the bands in a p-n-junction are offset, making a gradual transition from the p- to the n-region as seen in Figure 2.5b and 2.7 (a). The potential difference between the p- and n-regions is the built-in potential and equals the difference between the respective Fermi levels, i.e. $V_0 = E_{F_n} - E_{F_p}$ [18]. The built-in voltage depends logarithmically on the doping levels of the p- and n-type semiconductor [18, 19]:

$$V_0 = \frac{kT}{e} log\left(\frac{N_a N_d}{n_i^2}\right), \tag{2.1}$$

where N_a and N_d are the concentrations of the acceptor and donor, respectively, and n_i is the intrinsic carrier concentration. For Si at 300 K, n_i has the values $1.45 \cdot 10^{10}\ cm^3$. If the concentration of the acceptors is increased, the Fermi level

[3]The Fermi level is a concept from Fermi-Dirac statistics, defining the highest possible energy state for an electron at absolute zero temperature, where the electrons would be packed in the lowest available energy states allowed by the Pauli Exclusion Principle. At higher temperatures a certain fraction of electrons, characterized by the Fermi Function, are able to have energies above the *Fermi level*. It is often mentioned as the equivalent of the chemical potential of thermodynamics [17].

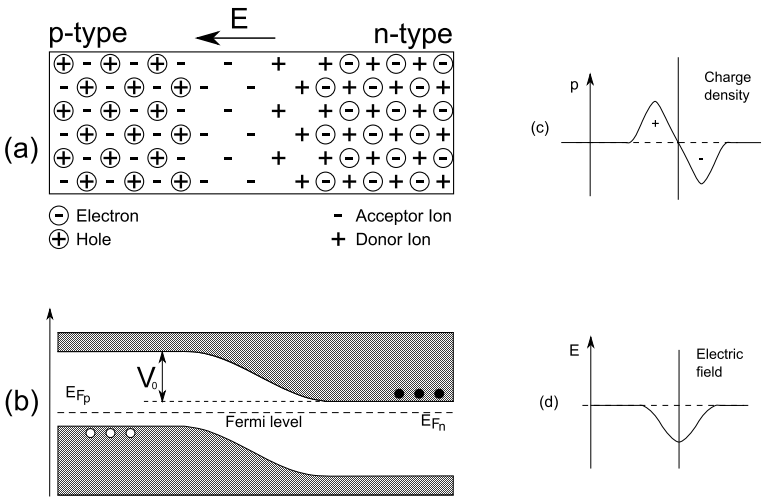

Figure 2.5: (a)Schematic diagram of an np junction, (b) diagram of electron energy levels showing creation of a contact potential V_0, (c) charge density, (d) electric field intensity [5].

will shift towards the valence band and if the concentration of donors is increased, the Fermi level will shift towards the conductive band.

The size of the space charge region is called the *depletion depth*. This depth is rather small for a semiconductor with no applied bias voltage (see Section 2.2.5) and depends on the concentration of the n- and p-dopants. Poisson's equation describes the potential of the space charge region [5, 18]:

$$\frac{d^2}{dx^2} = -\frac{\rho(x)}{\epsilon}, \tag{2.2}$$

where $\rho(x)$ is the charge density distribution in the zone and ϵ is the dielectric constant. Assuming the simple example of a uniform charge distribution about the junction, limiting the depletion region to x_n at the n-side and x_p at the p-side, yields:

$$\rho(x) = \begin{cases} eN_D & 0 < x < x_n \\ -eN_A & -x_p < x < 0, \end{cases} \tag{2.3}$$

where e is the charge of the electron. Due to total conservation of charge, we have:

$$N_A x_p = N_D x_n. \tag{2.4}$$

Integrating twice then yields [5]:

$$V_0 = \frac{e}{2\epsilon}(N_D x_n^2 + N_A x_p^2. \tag{2.5}$$

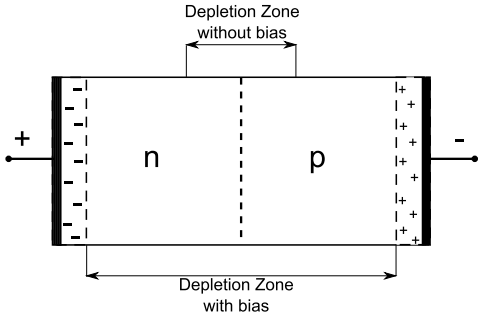

Figure 2.6: A reverse biased junction. The Depletion Zone is displayed with and without Bias voltage applied [5].

Using Equation 2.4 will lead to:

$$x_n = \left(\frac{2\epsilon V_0}{eN_D(1 + N_D/N_A)} \right)^{1/2}, \tag{2.6}$$

$$x_p = \left(\frac{2\epsilon V_0}{eN_A(1 + N_A/N_D)} \right)^{1/2}. \tag{2.7}$$

These equations demonstrate how the depletion zone stretches towards the lighter doped of the two sides if one side is heavier doped than the other [5]. The total width of the depletion zone is finally expressed as:

$$d = x_n + x_p = \left(\frac{2\epsilon V_0}{e} \frac{(N_A + N_D}{N_A N_D} \right). \tag{2.8}$$

2.2.5 Biased junctions

A simple device, as described in the previous section, will have a very small depletion zone. It will function as a detector but the operating characteristics are limited. The detector will not be able to provide an efficient charge collection and is limited to detecting low energy particles due to the low stopping power. The characteristics will improve if a *reverse bias voltage* is applied to the device. As seen in Figure 2.7c, the potential barrier is raised as a reverse bias is applied, reducing the electron and hole concentrations at the pn-junction and widening the depletion region [18]. The increase results from a negative voltage being applied to the p-side, attracting the holes in the p-region away from the junction towards the p-contact, and a positive voltage applied to the n-side has an opposite effect on the holes. As the voltage increases, the depletion zone grows, but at some point the semiconductors resistance is not high enough to withstand the increasing voltage, and the junction breaks down and starts conducting. The voltage required for the semiconductor junction to break down and start conducting is called the *breakdown voltage*.

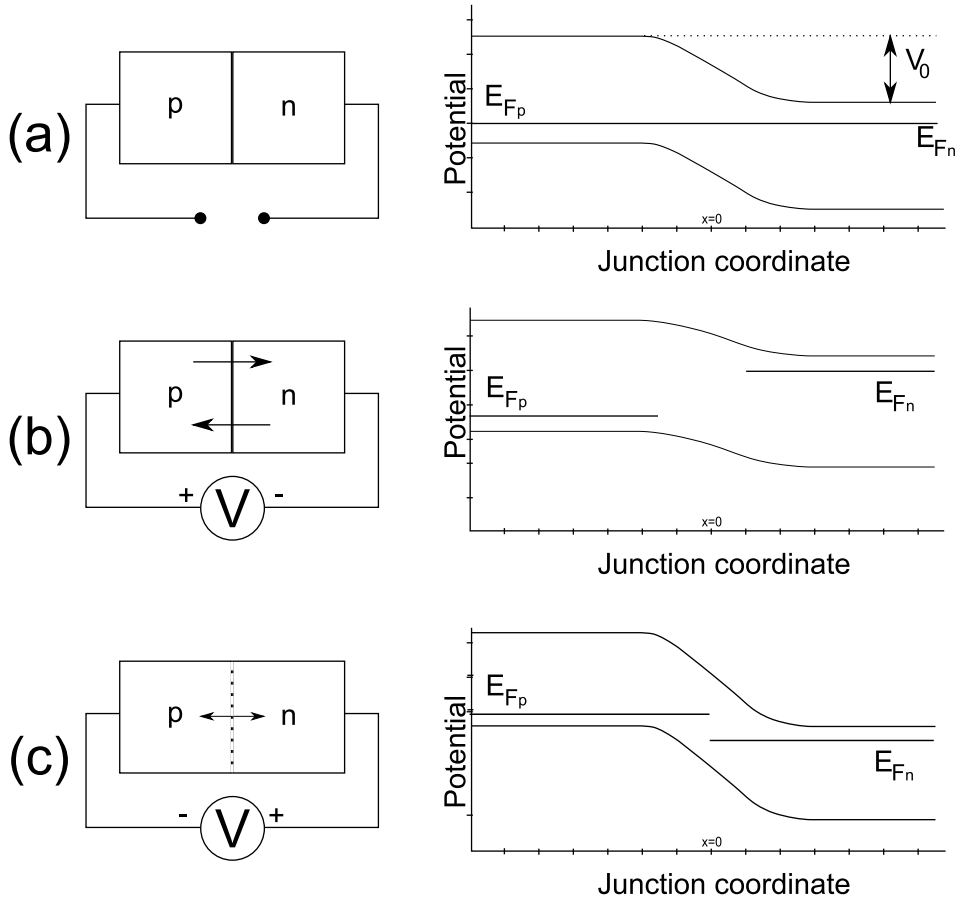

Figure 2.7: The pn-junction under various conditions. (a) Junction at thermal equilibrium. (b) Forward bias applied to the junction. This lowers the potential difference and increase the flow of electrons and holes through the junction. (c) Reverse bias applied to the junction. Potential barrier is raised, reducing the electron and hole concentrations at the pn-junction and widening the depletion region [18].

As there are no mobile carriers left in the depletion region, this volume forms a capacitator where the undepleted p- and n-regions act as the electrodes and the depletion region acts as the dielectricum. The depletion width increases with the square root of the reverse bias voltage, resulting in an increased sensitive volume and a reduction of the capacitance. For a charged particle traversing the detector this increases the signal charge and thus reduces the electronic noise, which is very beneficial [18]. The capacitance of a junction is defined as:

$$C = \epsilon \frac{A}{d} = A\sqrt{\frac{\epsilon e N}{2(V_b + V_0}}, \tag{2.9}$$

where V_b is the bias voltage and V_0 is the built-in voltage across the junction, N is the dopant concentration, ϵ the dielectric constant, A the area, e the electric charge of the electron and d the depletion depth.

2.2.6 Detection of charged particles and photons

Semiconductor detectors can be used both for the detection of charged particles and the detection of light. While a charged particle may cause a large amount of ionization events, or electron-hole pairs, as it traverses the semiconductor, a photon has a much shorter range and normally only produces one electron-hole pair. As a result the photodetectors will depend on ionization near the surface, while detectors used for charged particles or heavy ions are required to have a depletion region that is thick enough to stop all the incident particles. If the depletion layer is too small and some of the particles are not stopped, it will cause the response of the semiconductor to not be linear, as the entire energy of the incident particles is not deposited in the sensitive volume [5]. The main focus of this thesis will be the detection of photons, and the detection of charged particles will not be discussed further.

2.3 Photon Detectors

In the previous section, the concept of scintillating materials was introduced. Scintillators are often used in detectors in order to transform the energy of charged particles into light, which can then be detected by photon detectors. This section will discuss a few types of photodetectors that are commonly used for this purpose.

2.3.1 PhotoMultiplier Tubes

A photomultiplier tube (PMT) is a device that is commonly used in experiments where counting photons is desired. With extreme sensitivity, able to count even single photons, the PMTs can convert light into a measurable current. They have a high gain, low noise, a high frequency response and a large area of collection. A PMT is a vacuum tube consisting of an input window, a photocathode, focusing electrodes, an electron multiplier (dynodes) and an anode. When light enters the photomultiplier, it can excite electrons in the photocathode, resulting in

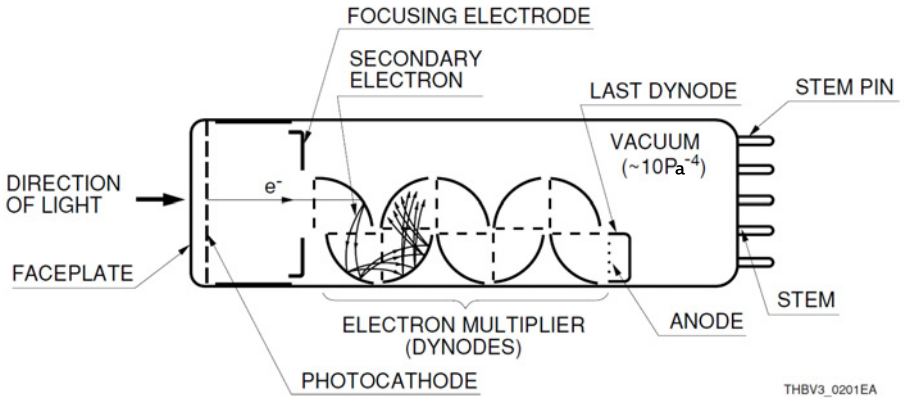

Figure 2.8: Schematics of a Photomultiplier Tube (PMT). The light enters the PMT through the window of the vacuum-tube, which contains a photocathode that will emit electrons when hit by an incident photon. The electrons are focused towards a set of dynodes, producing a cascade of secondary electrons in a multiplying process. These electrons are then collected at the anode and read out [20].

photoelectrons being emitted into the vacuum by the photoelectric effect. From there the photoelectrons are focused and accelerated towards the first dynode, where they are multiplied by secondary emissions. As there are several dynodes in the PMT, this multiplying process will repeat as the secondary electrons are created and accelerated towards the next dynodes, which cause a cascade of electrons that are collected by the anode as a signal (current). The quantum efficiency (the percentage of the light hitting the photocathode which will result in a released photoelectron) of a PMT is normally around 20-30% [21]. If the cathode and dynode systems are assumed to be linear, the current at the output of the PMT will be directly proportional to the number of incident photons [5], and the detector is said to be operated in the proportional mode. Connecting a PMT to a scintillator would then make it possible to determine the energy left in the scintillator by the incident particle, as the amount of photons produced in the scintillator is proportional to the energy deposited.

Various materials, which have different spectral responses, can be used as a photocathode in the PMT. In order to optimize the performance of the PMT, a suitable cathode material should be selected for the wavelengths of the light being measured. In addition, the window materials will often absorb ultraviolet radiation, so the window material will determine the short wavelength limit [20]. If possible, using a monochromator for selecting a narrow range of wavelengths will further improve the accuracy of the detector. The gain (current amplification) μ of the PMT is depending on the number of dynodes, their properties and the voltage applied over them. The secondary emission ratio δ is a function of the

applied voltage over the dynodes E and is given as:

$$\delta = a \cdot E^k, \tag{2.10}$$

where a is a constant and k is determined by the structure and material of the dynode, and has a value from 0.7 to 0.8 [20]. The photoelectron current I_k emitted from the photocathode will hit the first dynode, resulting in secondary electrons I_{d1} being released. By the first dynode, the secondary emission ratio δ_1 is given as:

$$\delta_1 = \frac{I_{d1}}{I_k}. \tag{2.11}$$

Following the multiplication process by the following dynodes, we have for the n-th dynode

$$\delta_n = \frac{I_{dn}}{I_{d(n-1)}}. \tag{2.12}$$

The anode current Ip is given by $I_p = I_k \cdot \alpha \cdot \delta_1 \cdot \delta_2 \cdots \delta_n$, where α is the collection efficiency. The product of $\alpha, \delta_1, \delta_2, ..., \delta_n$ is called the gain, μ. If we have a PMT with $a = 1$ and n dynode stages, operated using and equally-distributed divider, the gain μ changes in relation to the supply voltage V:

$$\mu = (a \cdot E^k)^n = a^n (\frac{V}{n+1})^{kn} = AV^{kn}, \tag{2.13}$$

where $A = \frac{a^n}{(n+1)^{kn}}$. It can thus be seen that the gain is proportional to the kn exponential of the supply voltage [20]. Despite the mentioned advantages of the PMTs there are also some drawbacks which limits their areas of application. A PMT is sensitive to magnetic fields, they are relatively large in size, require a high voltage for operation and has a rather low quantum efficiency as previously mentioned.

2.4 PIN diode

A simple version of the semiconductor detector is the PIN diode, commonly used for gamma spectroscopy. This detector consists of thin layer of a highly doped n-type (n^+)[4] with a high resistivity intrinsic layer is placed, followed by a thin, heavily doped, p-type layer (p^+). An example of a PIN diode can be seen in Figure 2.9. This type of diode has no intrinsic amplification and if, for example, a minimum ionizing particle crosses a depletion layer of $300\mu m$ (which should be sufficient to provide a useful detection efficiency up to 20-30 keV [21]) and produces about $3 \cdot 10^4$ electron-hole pairs, this will only correspond to a signal of $4.8 \cdot 10^{-15} C$ [3]. Since the PIN diode does not have any intrinsic amplification, it is therefore dependent on a charge sensitive preamplifier to amplify the signal, normally followed by a signal shaper.

[4]The notations such as p^+ and p^- indicates heavily or lightly doped regions, respectively. A moderately doped p-region will simply be denoted as p here. Similarly for the n-type doping, n^+ indicates a heavily doped region, n^- denotes a lightly doped region.

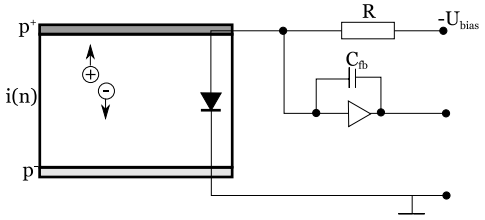

Figure 2.9: A PIN diode connected to a charge-sensitive preamplifier. [3]

2.5 Avalance Photo Diode (APD)

Even though a semiconductor detector can be used as it is without amplification for the detection of charged particles, many situations may make intrinsic (built-in) amplification of the detector desirable in order to acheive a high collection speed or low noise, e.g. for the detection of scintillating light. A common device with intrinsic amplification is the *Avalanche Photo Diode* (APD) which operates in a proportional mode, meaning that the signal obtained is proportional to the energy of the incident photons. The APD consists of a moderately doped p-type silicon base (p) upon which a junction of a lightly doped p-type (p^-) and a thin, highly doped n-type (n^+) layer is placed, as seen in Figure 2.10. A zoomed in view of the top region can be seen in Figure 2.11, along with the charge density ρ, electric field E and potential V of the section. As seen from the figure, the electric field peaks at the p-n^+ junction. In Figure 2.10 incident radiation, e.g. photons, results in an electron-hole pair being formed in the p^- region, which is separated by the electric field leading the electron towards the high-field region, while the hole drifts towards the bottom of the detector. As the electron is accelerated in the high-field region it may initiate *impact ionization*, creating a new electron-hole pair. This new pair will, in the same fashion as the previous pair, be splitted and the electron will be accelerated. The following avalanche of produced electron-hole pairs gives rise to the name of the APDs. This impact ionization is only possible if the electric field is strong enough to accelerate the electrons (and holes) enough to reach the threshold E_{th} before the next collision. An approximation of the production of secondary charged particles can be made by considering the *ionization rates* which characterize the impact ionization [22]. The ionization rates are defined as the probabilities of an impact ionization to occur per unit length, and is different for electrons and holes, denoted α_i and β_i, respectively. In order for an electron to obtain the energy $E_0 \approx E_{th}$, which is the characteristic critical energy, it has to move a distance

$$l_F = \frac{E_0}{eF}, \tag{2.14}$$

without colliding, where F is the electric field. The probability of such an event is:

$$p \approx exp(-l_F/l_0) \approx exp\left(-\frac{E_0}{eFl_0}\right), \tag{2.15}$$

where l_0 is the mean free path. The expressions for the ionization rates then takes the shape:

$$\alpha_i = \alpha_0 exp[-F_{n0}/F], \tag{2.16}$$
$$\beta_i = \beta_0 exp[-F_{p0}/F], \tag{2.17}$$

where $F_0 = E_0/el_0$. The experimental dependencies for α and β of the field, F, are usually described by the empirical equations [22]:

$$\alpha_i = \alpha_0 exp[-F_{n0}/F]^{m_n}, \tag{2.18}$$
$$\alpha_i = \alpha_0 exp[-F_{n0}/F]^{m_p}, \tag{2.19}$$

The coefficients are material dependent, and is, for example for Si, $m_n = m_p = 1$ and

$$\alpha_i = 3.318 \cdot 10^5 exp[-1.174 \cdot 10^6/F] \ (cm^{-1}). \tag{2.20}$$

The dependencies on F for α_i and β_i for many materials can be found in [23]. The ratio of the hole-to-electron ionization coefficients is called the k-factor or ionization ratio, $k = \beta_i/\alpha_i$ [24], and is a very important parameter of an APD as it determines its *multiplication noise*. The multiplication noise or *excess noise* is caused by the statistical nature of the multiplication factor, M, or gain, of the APD. M is given as the average number of electron-hole pairs per absorbed photon, but the actual value will naturally vary, leading to a fluctuation in the gain. The multiplication gain can be given as [25]:

$$M(x) = \frac{exp\left[-\int_x^w (\alpha - \beta)dx'\right]}{1 - \int_0^w \alpha exp\left[-\int_{x'}^w (\alpha - \beta)dx''\right]dx'}, \tag{2.21}$$

where w is the width of the high field avalanche region. The k-factor is, similarly to the ionization coefficients, dependent on the electric field, F, and the semiconductor material. If the reverse bias voltage, and thus the electric field, is increased both the multiplication gain and noise will increase. The excess noise factor, F_{ENF}, is given as:

$$F_{ENF}(M) = M\left(1 + \frac{1-k}{k}\left(\frac{M-1}{M}\right)^2\right) \tag{2.22}$$

This equation shows how the excess noise will vary due to the ionization ratio. A plot of how the excess noise factor responds to various coefficient ratios can be seen in Figure 2.12. When an equal amount of electrons and holes are produced, i.e. $\alpha = \beta$, k = 1 and the excess noise factor will be at its maximum. For decreasing values of k the excess noise factor will decrease as well. This is valid both for high ratios of the electron or hole coefficients[5].

[5]The ionization ratio can also be written as α_i/β_i in the case where more holes than electrons would be produced. The probability of electrons and holes to initiate impact ionization is not equal and depends on the material, e.g. for Si electrons are much more likely to initiate impact ionization than holes are [28].

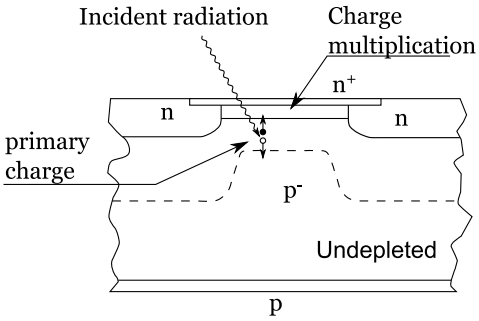

Figure 2.10: A cross-section of an avalanche photo diode (APD) consisting of a p-type silicon layer, upon which a moderately doped p-type layer and a heavily doped n-type top layer is placed [26].

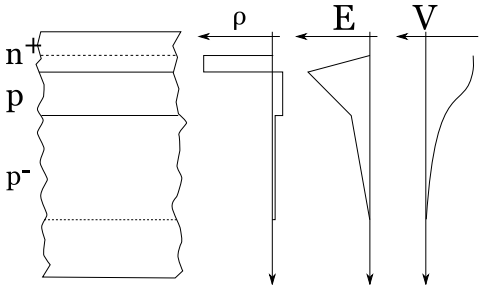

Figure 2.11: A zoomed in version of the APD shown in Figure 2.10. The curves display the charge density, ρ, the electric field strength, E, and the potential, V, of the section. The curves are aligned with the different layers of the APD in order to give a representation of how the various parameters vary throughout the detector [26].

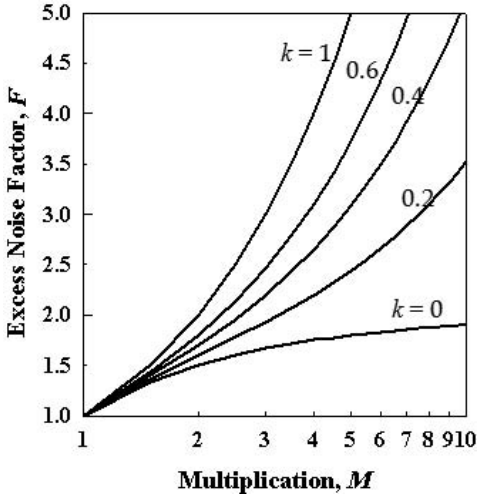

Figure 2.12: Plot of the excess noise factor, F, as a function of the multiplication, M, for different values of the ionization ratio, k. For lower values of k, i.e. a large fraction of one type of charge carrier compared to the other, there will be a much lower noise for high multiplication gains [27].

2.6 Geiger-mode Avalanche Photo Diodes (G-APDs)

The analogy of the gas-ionization detectors and semiconductors was used earlier in this text, and when the topic of *Geiger-mode APDs* is being discussed it can again be explained by comparing to the gas-ionization detectors. If the applied voltage to such a detector is increased, the detector will go from a simple recombination region at low voltages (gain is equal to 1), pass on to the ionization region, further to the proportional region before it reaches the Geiger-Müller region at even higher voltages. As the Geiger-Müller region is reached the signal saturates, and even if the incident radiation is increased further, the signal out will not increase.

Returning to the APD, the Geiger mode occurs when the reverse bias voltage is raised above the breakdown voltage. Since the voltage is increased, both electrons and holes will initiate impact ionization to a higher degree. The increased energy field enables the charge carriers, i.e. the electrons and holes, to gain the required energy more easily before the next collision. As the charge carriers are at average produced at a higher rate than they can be extracted, the detector can be said to have reached the *avalanche breakdown voltage* [28]. This results in an exponential growth of charge carriers. Increasing the reverse bias voltage will reduce the time constant of the growth. If the detector is connected in series with a resistor, the increased current will result in a voltage drop over the resistance, which will in turn reduce the voltage drop over the high-field region of the detector and slows down the rate of growth of the avalanche. This is because resistance works as a simple negative feedback system for the system which only allows the avalanche

to grow to a certain limit set by the resistor. As the voltage is reduced back to the breakdown voltage, the generation and extraction rates will be in balance and the system stabilized by the resistance. If the current decrease, there will be a reduced voltage drop over the resistance, and similarly for an increase in the current will cause the voltage drop to increase.

In order to be able to detect a new incident particle, the detector has to be shut down [28]. In order to stop, or *quench*, a G-APD, there are two possibilities. The first possibility is *passive quenching* where the detector is charged up to a certain bias voltage above the breakdown level. When an avalanche is triggered it will then increase the current until it discharges its own capacitance and is dropped below the breakdown voltage and the avalanche dies out. The other possibility is *active quenching*, where an external system senses when an avalanche-event is starting in the detector, and then discharges the APD below the breakdown voltage by switching it off. The accumulated charge in the capacitance of the detector volume (see Section 2.2.5), is given as [29]:

$$Q = C(V_{bias} - V_{breakdown}), \tag{2.23}$$

where V_{bias} is the bias voltage, and $V_{breakdown}$ is the breakdown voltage. The gain is defined as the ratio between the accumulated charge and the electron charge, which is the charge of one electron:

$$G = \frac{Q}{q_e} = \frac{C(V_{bias} - V_{breakdown)}}{q_e}.. \tag{2.24}$$

In these detectors the current signal given is no longer proportional to the energy of the incident radiation, but rather functions as an event-detector. Such a detector will only tell you whether an event has occured or not, but does not provide any sppecific information about it, such as the energy of the incident particle. It is therefore useful for example as a photon counter in extremely low-light applications.

2.7 Multi-Pixel Geiger-mode Avalanche Photo Diodes

In the previous section the concepts of the Avalanche Photo Diode (APD) and the Geiger-mode APD (G-APD) were discussed. A newer addition to the range of semiconductor detector uses the same principles as the G-APD, and simply arranges the detectors in arrays, namely the The Multi-pixel G-APD (MAPD). A single G-APD functions as a digital 2-bit counter, as it detects if there is an event or not. The detector does not yield any information about the event except for its existence and thus has a limited field of applications. Each G-APD in the array is referred to as a pixel, and the number of pixels in a MAPD can be in the order of magnitude ranging from 100 to $10^4/mm^2$. The benefit of having an array of pixels, instead of just one single G-APD pixel, is that the dynamical range (see Section 2.7.4) is increased drastically by increasing the number of pixels.. Due to

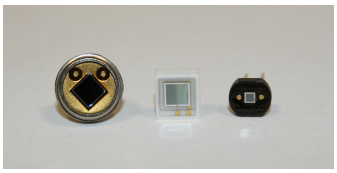

Figure 2.13: This picture shows various types of MAPD. From left to right: MAPD3-A from Zecotek (identical design as the MAPD3-N), MPPC S10362-33-050C and MPPC S10362-11-025C from Hamamatsu.

the extensive research and improvements on MAPDs since they were first invented, they have now begun to replace both photomultiplier tubes (PMTs) and APDs for many applications. Some benefits of the MAPDs are:

- Operates at a low bias voltage (often less than 100 V).
- Insensitive to magnetic fields up to ∼15 Tesla [30].
- High gain $\sim 10^4 - 10^6$ (PMTs also have high gains, around $10^6 - 10^7$).
- Shows no aging [30], however radiation damage may occur, damaging the structure to some degree, causing increased leakage current and dark count rates [31].
- High Quantum Efficiency, typically 80% for the entire wavelength range of visible light [30].
- Very good timing resolutions.
- Excellent sensitivity and resolution for single photons.
- Potentially low cost.

2.7.1 Different types of Multipixel G-APDs

There are different types of MAPDs being developed and produced by companies, e.g. the multipixel photon counters (MPPC) from Hamamatsu, the MAPD from Dubna and the MAPD3-N from Zecotek. There are some variations in how there are built, which naturally has an effect on the characteristics. The detectors presented in the following sections are all G-APDs, but their names vary from company to company.

2.7.2 Silicon Photomultiplier (SiPM) and Multi Pixel Photon Counters (MPPC)

SiPM and MPPC detectors has a very similar topology. These detectors are multipixel Geiger-mode semiconductor photodiode with about 100-4000 pixels per mm^2, or a pixel size of about 15-70 μm, joint together on a common silicon substrate. Each pixel is quenched by an external resistor R, with typical values of

about 100-200 kΩ [32]. This resistor connects the pixel to a common conductive grid. Every hit in a single pixel will yield the same shape and charge, even if there is only one or several photons hitting the pixel at the same time [33]. This naturally gives some uncertainty, which will be discussed in Section 2.7.4. The signal for the entire detector will be the sum of the signals from each pixel. If the incident light is not too intense, this output signal will be proportional to the number of photons hitting the device, as each pixel is assumed to receive a maximum of 1 photoelectron (p.e.) within the recovery time of the pixel (Section 2.7.4). This gives an obvious improvement from the G-APDs, which have no dynamical range. The typical gain of a SiPM lies in the range of $10^5 - 10^6$, which reduces the need for very advanced pre-amplifiers as is needed for detectors with no intrinsic gain.

SiPM Topology

Figure 2.14a shows an example of a SiPM detector, where a single pixel is in the center of the picture. In Figure 2.14b a cross-sectional view of a SiPM can be seen, displaying the internal structure of a single pixel. A few micron epitaxy layer on a low resistive p substrate forms the drift region with a low built-in electric field (the field is shown in Figure 2.14c). In the upper part of the pixel there is a thin depletion region of about $0.7 - 0.8\ \mu m$ in the junction between the p^+ and n^+ layers, where there is a very high electric field of 3-5·10^5 V/cm. This is the region where the avalanche will take place during an event [32]. n^- guard rings separate each pixel, and the connection to the common Al-conductor (shared by all the pixels and which the signal is read out from) is made through the polysilicon resistive strips. As can be seen from the images in Figure 2.14, there is a dead space between the pixels. This lowers the geometrical efficiency, $\epsilon_{geometric}$ (see Section 2.7.4), i.e. the fraction of the total G-APD area occupied by active pixel areas, and hence also the probability for an incident photon to produce a detection event. The effective area of a SiPM is about 25%-60% [34].

2.7.3 Micro-pixel APD

Zecotec Photonics have produced three types of MAPD detectors, based on the same structure but with various properties due to improvements and developments. These detectors are named MAPD-3A, MAPD-3B and MAPD-3N. The MAPD-3A has a pixel density of 15000 mm^{-2} and the MAPD-3B has a pixel density of 40000 mm^{-2}, both of them with a total active area of 3x3 mm^2, a PDE of about 10% and a pixel gain[6] of about $2 \cdot 10^4$ for the MAPD3-A, and $1 \cdot 10^4$ for the MAPD3-B [35, 36]. The MAPD3-N is the newest of the devices and has a pixel density of 15000 mm^{-2}, and an active area of 3x3 mm^2 [37]. The MAPD3-N is expected to have a gain in the order of 10^4. The MAPD3-N is a rather new detector, so the characteristics are not yet widely tested. This thesis aims to characterize some of the properties of this detector, and the results will be discussed in Section 5.

[6] The gain varies with the bias voltage.

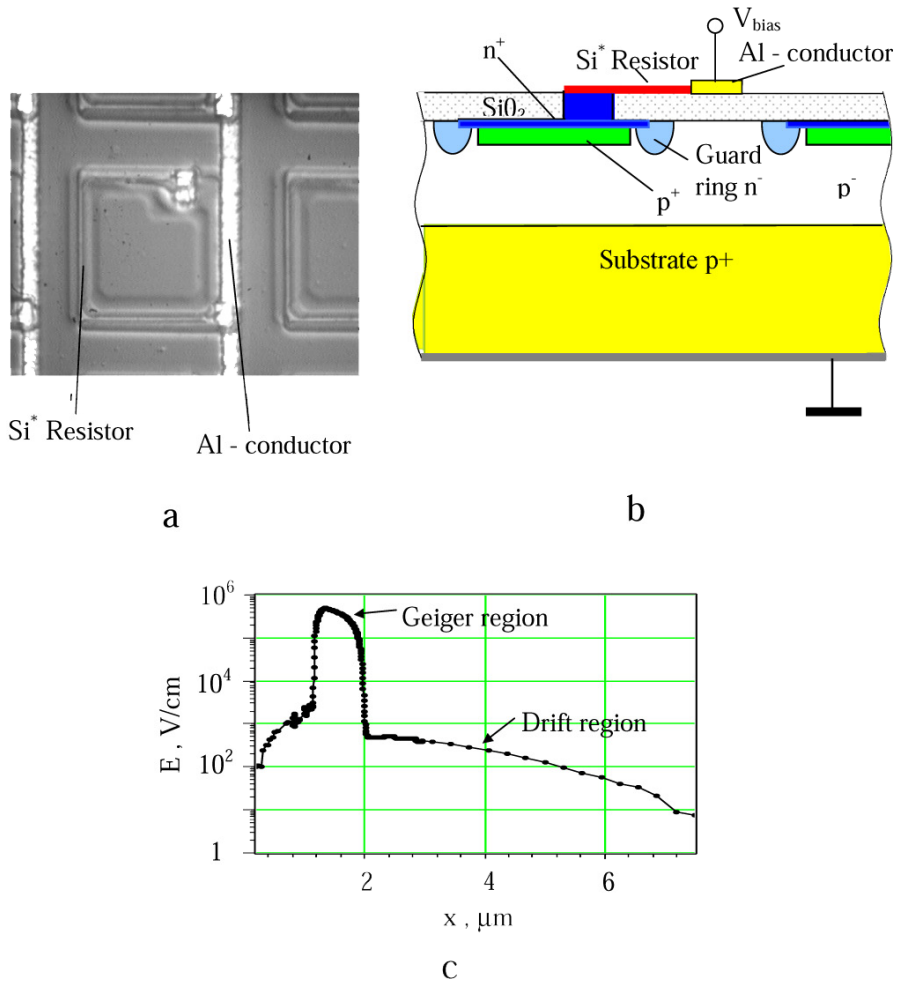

Figure 2.14: (a) Micro-photograph of a SiPM. (b) Cross-sectional view of a SiPM. (c) Electric field distribution in the epitaxy layer [32].

MAPD Topology

In the same way as the SiPM, the MAPD consist of several pixels arranged in an array. A major difference from the SiPM, however, is that the pixels of the MAPD are deeply buried micro-wells of vertical p-n-p-n structures, as opposed to the pixels of the SiPM which lie near the surface of the detector [38]. The topology of the MAPD and its energy zone diagram can be seen in Figure 2.15. The detector consists of a low resistivity n-type silicon wafer, upon which a n^+ layer is placed, and a epitaxial p-type layer of $\sim 8\ \mu m$ is grown. The n^+ and epitaxial layer create a flat p-n junction together. In the middle of the epitaxial layer there are several n-type pixels organized in an array, which creates a p-n junction with the epitaxial layer. At the very top of the detector there is a p^+ layer [38]. The first p-n junction (from the top), is the avalanche region and it is reverse biased. The next junction, the n-p junction between the pixel and the epitaxial p layer is then forward biased and acts as a potential well of about 0.5-0.7 V, in which the multiplied electrons are collected. After a few nanoseconds of accumulation there will be a sharp decrease in the electric field in the avalanche region, i.e. the first p-n junction, which results in the avalanche process being quenched. Within a few tens of nanoseconds the avalanche process is stopped and the accumulated electrons drift into the substrate due to sufficient leakage of the third p-n junction, and thus the independent multiplication channels, or pixels, do not have charge coupling between them [38]. A great benefit of the deeply buried microwells compared to the pixel structure of the SiPMs is that there is no dead space between the pixels in the MAPD-layout, giving an effective area of 100%, compared to the 25%-60% of the SiPM.

2.7.4 Characteristics of Multipixel G-APD

When working with Multipixel G-APDs, such as the MPPC, SiPM and MAPD, it is important to be aware of the characteristics of the detector. This section will discuss some of the most important parameters one should keep in mind.

Photon Detection Efficiency (PDE)

The Photon Detection Efficiency (PDE) is the probability that a photon will produce a detection event in the detector. The PDE is wavelength dependent due to the design of the detector, especially due to the combination or the order of the p and n layers. In silicon, free electrons have a higher probability to trigger a breakdown than holes. Therefore, the creation of free carriers in a front p-layer of the G-APD has the highest probability to initiate a discharge. Devices which are made of p-silicon on an n-subtrate are sensitive to blue light, which is absorbed in silicon within a fraction of a micrometer [39]. In devices with n-silicon on a p-substrate, the light has to pass through the n-layer to generate an e-h pair in the underlying p-layer, where the electron has a much higher probability of starting the breakdown than in the n-layer. Only light with a wavelength longer than 500 nm has an absorption length longer than 1 μm, the typical thickness of the minimum layer of the high field zone. This leads to a PDE peak around 600 nm

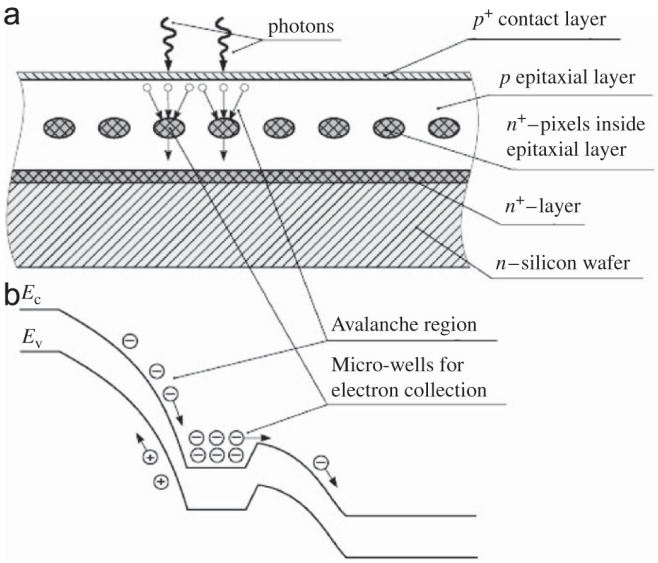

Figure 2.15: (a) Cross-sectional view of a MAPD, displaying the structure with deeply buried, individual microwells. (b) Energy zone diagram of MAPD [38].

or higher for such designs [39]. The PDE is given as:

$$PDE(\lambda) = QE(\lambda)\epsilon_{geometry}\epsilon_{Geiger}(\lambda), \tag{2.25}$$

where $QE(\lambda)$ is the quantum efficiency, or the probability that the photon is absorbed in the active region of the diode (typically 80% for the whole wavelength range of visible light [30]). $\epsilon_{geometry}$ is the geometrical efficiency, describing the fraction of the total area of the diode occupied by active cell areas. ϵ_{Geiger} is the probability for a carrier created in the active cell volume to initiate a Geiger-mode discharge [39], and strongly depends on the bias voltage applied and the wavelength of the light.

Absolute Gain

MAPDs operate in the Geiger mode and the amplitudes, A_i, of the individual cells depend on the applied overvoltage, ΔV, and the cell capacitance, C:

$$A_i \sim C \cdot \Delta V = C(V_{bias} - V_{breakdown}). \tag{2.26}$$

When many cells fire at the same time, the output amplitude is the sum of the standard pulses of the individual cells:

$$A = \sum A_i. \tag{2.27}$$

Dynamical Range

The dynamical range of a MAPD is limited by the number of pixels of the device. In an ordinary G-APD there is only one pixel, which does not discriminate between the amount of incoming light, it simply records an event as on or off. The same thing happens in a multi-pixel G-APD, but in this case there is a high number, m, of pixels which each will produce a signal which are added together to provide the total signal of the detector during an event. The higher pixels density, the more individual photons can be detected at the same time. However, if the flux of photons incident on the detector is too high, the same problem as with the single G-APD may occur, namely that more than one photon hit the same pixel before the pixel has had time to recover after the previous event. For low fluxes of photons, the output of the detector is proportional to the number of incident photons, as it is assumed that only one photon hit each pixel per recovery time. For higher fluxes, where some cells may be hit by more photons, the response is nonlinear and at even higher fluxes the detector will be saturated, meaning that a large fraction of the pixels are fired, and increasing the input will no longer increase the output signal. The number of fired pixels N_s depends on the number of photoelectrons created N_{ph} [35]:

$$N_s = N_{pix}\left[1 - exp\left(\frac{N_{ph}}{N_{pix}}\right)\right], \tag{2.28}$$

where N_{pix} is the total number of pixels in the array. This approximation is only valid if the duration of the light pulse is shorter than the recovery time, τ_{rec} of a pixel. If an ideal MAPD under ideal light conditions is considered, that is a MAPD with an excess noise factor equal to unity with no crosstalk between the cells (a single photon only triggers one cell) and where each incident photon hits a cell, the intrinsic amplitude resolution can be found. This intrinsic resolution is the minimum resolution possible for the detector, and can be shown to be $R = 2.35 \cdot \sigma/\bar{\mathrm{A}}$, where A is the amplitude of the detector response, and $\bar{\mathrm{A}}$ and σ are the mean value and standard deviation characterizing the distribution of A (which is assumed to be normal) [40]. This shows that due to statistical noise in the process of distributing n photoelectrons over m cells, the resolution has a lower limit.

Inter-cell crosstalk

During the breakdown of the cell in a MAPD, a micro-plasma is created and electrons are lifted to high bands, which causes photons to be emitted when the electrons return to lower states [30]. If these photons have a high enough energy they can travel to a neighbouring cell and trigger a new breakdown in that cell. This process cause a small additional contribution to the readout signal, and contributes to the excess noise factor as it is a stochastic process. The crosstalk can be greatly reduced by optical isolation in the trenches between the cells. Unfortunately this takes up space and thus reduces the PDE due to an increased dead space in the detector [30].

Recovery time

The recovery time of a MAPD is the time it takes for the detector to be ready to detect a new event after an avalanche process. This time depends on the capacitance of the pixel, C_{pixel} and the resistance of the quenching resistor, R. The recovery time is given as [35]:

$$\tau_{rec} = C_{pixel} \cdot R. \tag{2.29}$$

The recovery time shows a high dependence of the bias voltage and temperature of the detector. The temperature dependence can be seen as a result from the increased resistivity of the quenching resistors, and if the temperature decreases, the recovery time increases. The dependence of the bias voltage can be explained by an effect called *afterpulsing*, which interrupts the recovery of a cell after a breakdown and restarts the avalanche [41].

Dark count rate

The dark rate of a detector is signals caused by other effects than the creation of charge carriers by incindent radiation. The dark counts in a MAPD can exceed 1 MHz/mm^2 [30]. There are two main reasons for the dark count rate in G-APDs, namely thermal generation and field-assisted generation (tunneling) of free carriers. Of these two effects, the thermal one is the dominant and can be reduced by cooling. The dark count rate also decreases by increasing the threshold of the readout electronics [30]. The thermal generation is caused by carriers generated thermally in the sensitive volume of the detector, and they can not be distinguished from carriers generated from photons, and they will also be able to induce avalanches.

The dark count is mostly important when considering low intensities. When considering high light intensities, the dark count will have a limited effect, as this will be a very small part of the output signal. Increasing the threshold of the readout electronics will decrease the dark rate, but is mostly an option for applications where many photoelectrons are produced. Lowering the bias voltage will decrease the dark rate, but this will also decrease the gain and PDE of the detector, so considerations should be taken in order to balance the noise with the signal. The second source, i.e. the field-assisted tunneling, is caused by an excess of filled traps (compared to its steady state value) immediately after a breakdown. When the electron is excited out of the valence band and into a mid-gap trap state, a mobile hole is generated in the valence band. If the electron manages to tunnel out of the trap and into the conduction band before recombining with a hole in the valence band, it can be seen as if a new electron-hole pair has been generated (as opposed to a recombination where the system is reset to its original state) [42]. The trap has a tunnel lifetime since it is not a stationary state. This lifetime depends highly on the trap depth and the applied electric field, as these variables determine the depth and width of the potential barrier separating the trap from the conduction band [42,43]. The field-assisted tunneling can be reduced by cooling the device.

Chapter 3

Application

3.1 Projectile Spectator Detector (PSD)

The NA-61/SHINE experiment at CERN is an experiment meant to study the production of hadrons in various collisions, such as nucleus-nucleus, proton-proton and hadron-nucleus collisions. The nucleus-nucleus collisions may allow to study the critical point of strongly interacting matter. NA-61 is an upgrade from the earlier NA-49 experiment, and one of the main upgrades is the construction of a projectile spectator detector (PSD). The PSD will measure the number of non-interacting nucleons from a projectile nucleus in nucleus-nucleus collisions on an event-by-event basis [44]. A precise knowledge of the fluctuations caused by variations in the number of interacting nucleons, the collision energy, centrality and the size of the colliding nuclei is important in order to study the properties of the onset of deconfinement and to analyze the critical point of strongly interacting matter. The PSD is a very forward hadron calorimeter, placed 20 meters downstream from the target. Due to the spread of the projectile spectators the PSD is required to have a large front (traverse) size of approximately 2 m^2. The PSD also needs a high energy resolution ($\sim$ 50 $\%/sqrt(E)$) of the total energy of the projectile spectators in a wide energy range from 10 GeV to 30 TeV. In calorimeters based on scintillation read out it has traditionally been common to use PMTs for reading out the light, but the PSD has decided to take MAPDs in use instead, due to their small size, good PDE, simplicity of operation and a gain comparable with normal PMTs [45].

The PSD has a modular design which gives the possibility of optimization of the detector geometry in respect to various parameters such as the collision energies, distance from the collision point and changes in the magnetic field etc. [44] The final structure will consist of 108 individual modules, each with the transverse dimensions 10x10 cm^2. Each module will consist of 60 layers of lead-scintillator tile sandwiches with a 4 to 1 ratio of lead and scintillator plates (16 mm thich lead plates and 4 mm thick scintillator tiles). This results in a total length of about 120 cm, corresponding to $\sim$ 6 nuclear interaction lengths [45]. The scintillator tiles contain 1.1 mm thick circular grooves where a wavelength shifting fiber (WLS) is

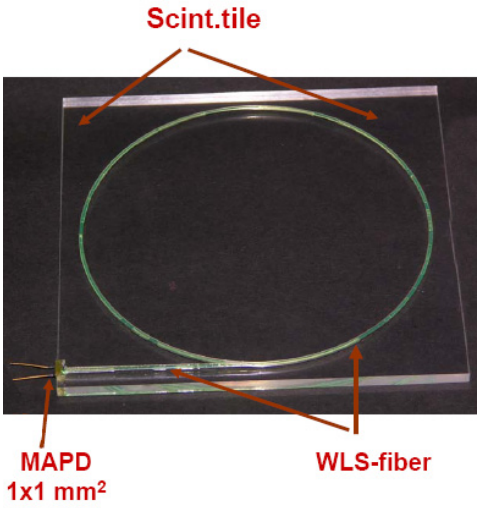

Figure 3.1: A scintillation tile with a WLS fiber inserted. The read-out is provided directly by a MAPD in the figure while the PSD will read out 6 WLS fibers per MAPD. Figure from [44].

placed, as seen in Figure 3.1. The WLS fibers are extended to the back end of the module where 6 WLS fibers are read out by a single 3x3 mm^2 MAPD. This results in a need for 10 MAPDs to fit at the back of each module, making the compact size of the MAPD ideal. Figure 3.2 shows the general structure of a single module.

Beam tests have been performed with the first supermodule, containing an array of 3x3 modules, at a hadron beam at SPS, CERN [45]. Initially each readout channel was calibrated by a muon beam, scanning all nine modules. After this was performed and the calibration coefficients were obtained, the supermodule was irradiated by a pion beam at 5 different energies in the range of 20 to 128 GeV. A spectrum of the deposited energy in the first section of the central module at 30 GeV can be seen in Figure 3.3 [45]. The dependence of the obtained energy resolution on the beam energy can be seen in Figure 3.4. From the fit in the figure, made from 5 points of experimental data, it can be seen that there is a stochastic term of 55% and a constant term of 3.6%. Adding a third term in order to compensate for shower leakage of about 16%, due to the relatively small size of the supermodule, yields a stochastic term of 53.5% and a constant term of 1.9% for a fixed leakage term of 16% [45].

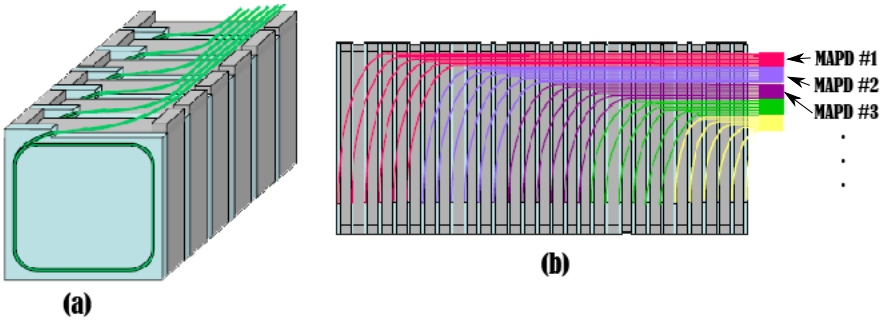

Figure 3.2: Illustration of the structure of a PSD module, and the layout of the WLS-fibers. The colours added to the WLS fibers in the figure illustrates how 6 consecutive tiles are read out by one single MAPD.

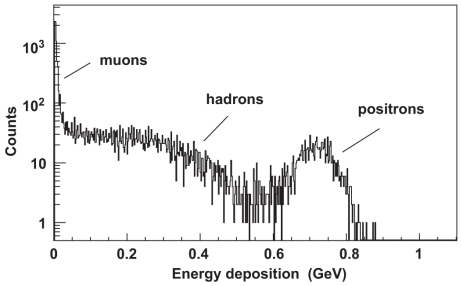

Figure 3.3: Spectrum of energy depositions in the first section of the central module from a 30 GeV pion beam that contains the fractions of muons and positrons [45].

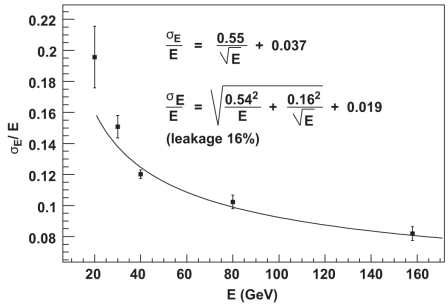

Figure 3.4: Dependence of the calorimeter prototype energy resolution on the beam energy. The upper equation is the parametrization of experimental points with a two-term formula. The lower expression includes the leakage term, and the curve for this relation can be seen as the solid curve in the figure [45].

Chapter 4

Experimental setup

4.1 The setup

When working with the characterization of a MAPD detector system the output signal received from the device will be weak, making amplification nessecary before it is read out by an analogue to digital converter (ADC). It is important to shield the system to prevent noise since any noise picked up between the MAPD and the pre-amplifier will be amplified along with the signal, potentionally drowning the signal. This chapter will discuss the setup used for performing various measurements, and discuss some of the actions taken against noise in the system. An image of the laboratory setup can be seen in figure 4.1.

4.1.1 Noise reduction

Preventing the noise in measurements is important in order to obtain good results. The focus of the work performed in this thesis has been to measure the characteristics of the MAPD3-N detector, which has an intrinsic gain in the order of 10^4. This is about one order of magnitude below other multi-pixel G-APDs, such as the SiPM, which has a gain in the order of 10^5 to 10^6. Since the signal is one to two orders of magnitude weaker, it is obvious that less noise is needed to drown the signal. Observing the peaks of few photoelectrons in the detector is required in order to determine the gain (see Section 4.2.2), making it important to be able to distinguish these weak signals from the noise.

The sensitive parts of the measurement setup have been placed in a aluminium box which will be referred to as the black box. The black box can be seen in Figure 4.1, and consists of a simple aluminium box with a lid. When the lid is placed over the box, its edges will overlap with the walls of the box itself, preventing light from slipping in through any gaps between the box and the lid. The inside of the box is covered in black clothing in order to reduce light pollution of any stray light inside the box. To ensure good shielding it is important that both the box and its lid are connected to a common ground. If the lid is not connected to the common ground, it will allow electromagnetical signals to pass through it.

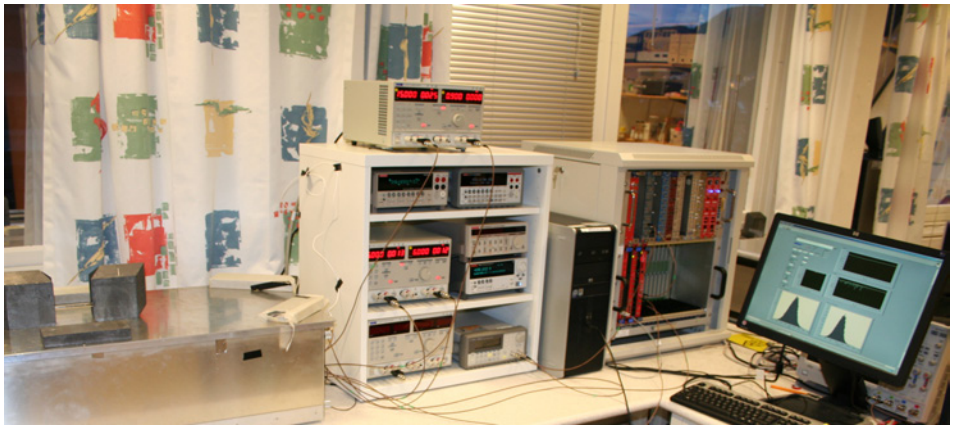

Figure 4.1: Image of the entire lab setup. The large aluminium box to the left is the black box, upon which a few lead weigths are placed.

In order to improve the connection between the lid and the box a strip of copper wiring have been placed on the surfaces where the lid rests upon the box. In order to provide good contact between these layers, lead weights were placed on top of the lid around the edges to help pushing the lid down[1]. Any cables going into the box by simply putting them over the edge of the box (i.e. between the box itself and the lid) would function as an antenna, picking up noise from the surroundings and bringing them into the box. This would then cause noise in the system, and the box could not be considered to be properly shielded any longer. To solve this problem the box is equipped with several connectors on its side where shielded cables can be connected by BNC or LEMO connectors (see Figure 4.2). These connectors will then have a common ground as they are connected to the chassis of the box, and the cables connected to the box through these will no longer bring noise from the outside into the box. At the moment of the experiment there was one cable (the thermistor cable) which was not connected in this way, but instead was placed over the edge of the box. To ensure that this would not have any negative effect on the system, it had to be connected to the same common ground as the others. This was done by removing a small piece of the outer plastic insulation of the wire, which reveals the shielding of the cable. This shielding was then connected to the chassis of the box with aluminium tape, ensuring a good connection to the common ground, i.e. the chassis of the box, as can be seen in Figure 4.2.

One of the major improvements of the signal to noise ratio from the setup, previously used by A.T. Samnøy [2] and H.A. Erdal [1], was a replacement of the pre-amplifier and read-out circuit. Previously the readout and pre-amplifying was done seperately. The SiPM was connected to a box providing the bias voltage,

[1]The lead weights did not decrease the noise by a large amount, but were added in the process of optimizing the noise reduction, especially in regard to the attempt of measuring the dark rate (Section 4.2.3). This also provides for a more stable setup

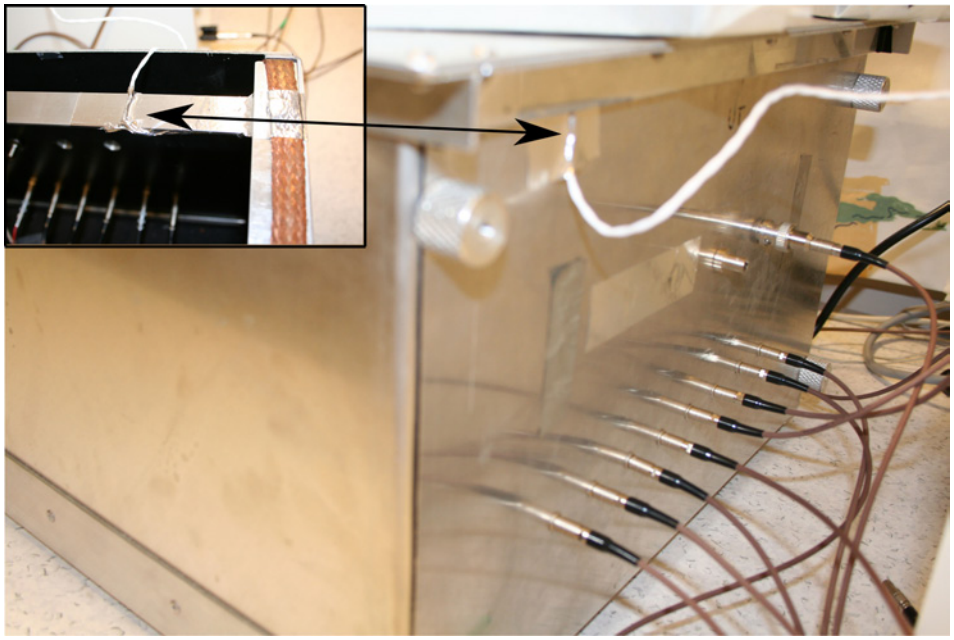

Figure 4.2: Image of the connectors on the side of the black box. In the top left corner, the connection of the thermistor cable can be seen. The cable is a twisted pair cable, with a shielding connected to a copper plate which is placed at the MAPD. The isolation of the cable has been stripped at the area under the aluminium tape, which enables the connection to the common ground of the black box chassis. The copper strip to the right in the small image provides good contact between the lid and the chassis, in order to connect the lid to common ground as well.

and the signal would be sent to a pre-amplifier in a separate box as seen in Figure 4.3a. This pre-amplifier amplified the signal by a factor 100, and send it to the ADC. The new pre-amplifier is a combined read-out and amplifying circuit, all placed in the same box, as seen in Figure 4.3b. This pre-amplifier is a charge sensitive amplifier (current to voltage) made by Victor Marin at the Institute for Nuclear Research (INR) in Moscow. Scientists from INR are currently also working with the characterization of the MAPD3-N as they are involved in the Projectile Spectator Detector (PSD) at the NA-61 experiment at CERN, where the MAPD3-N will be used for scintillation readout (see Section 3.1). This pre-amplifier has been designed keeping the MAPD3-N in mind, which means it provides a very low noise and a gain of ~ 197 (see Appendix A for specifications).

The LED-pulser is one of the main contributors to noise within the black box. The pulser switches on and off rapidly to provide the short pulses of light required by the system. Changes in the current running through the wires and circuits of the pulser will cause interference noise to the other devices in the black box. To reduce the impact of this noise the pulser has been put at a distance from the

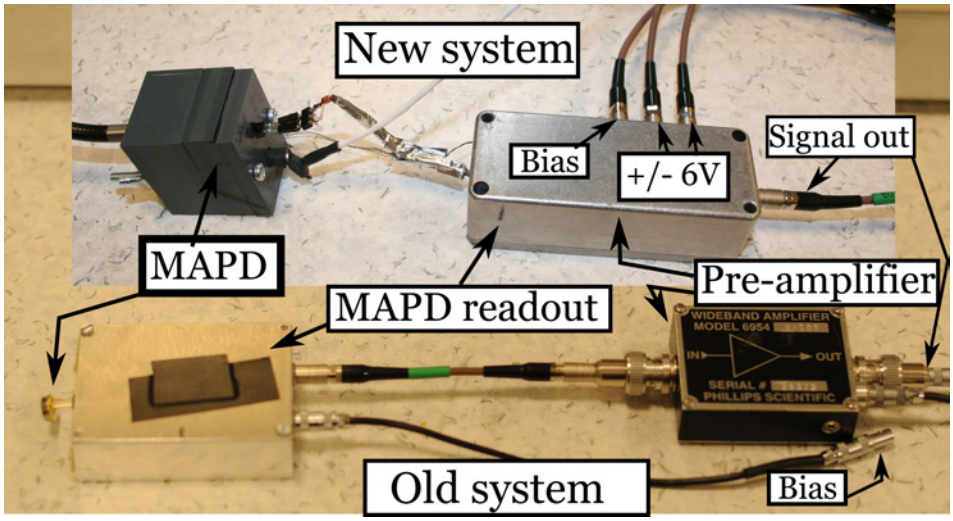

Figure 4.3: The old and the new readout and preamplifier system. The new preamplifier reads out the signal and amplifies it within the same shielded box, the old system uses two separate boxes for the task.

MAPD in the black box. Any other cables with signals that alternate during the measurements should always be kept as far away from the detector as possible. It was discovered that the circuit within the aluminium chassis of the LED-pulser was not properly grounded, and at while moving the pulser (e.g. when disconnecting the wires and reconnecting them) the noise of the system could increase severely. In order to reduce this noise, aluminium tape was used to connect the ground of the circuit to the chassis of the pulser and to its connectors. In this way common ground was provided through a simple but efficient solution. A comparison of the noise before and after this was done can be seen in Figure 4.4. There have also been minor changes in the noise levels due to small variations in the setup, e.g. while moving components or wires in the setup. To limit these variations a LabVIEW VI was used to monitor the noise of the system in real-time, allowing the user to see how any changes would change the noise level, and thus limit the noise to a minimum before starting a measurement.

MAPD3-A v.s. MAPD3-N

At the start of the work presented in this thesis, the possibility of characterizing both the MAPD3-A and the MAPD3-N was considered. Previous attempts to characterize the MAPD3-A in Bergen have not been accomplished due to a limited signal-to-noise ratio. Despite the efforts made to reduce noise in the system, the few photoelectron peaks could not be observed for the MAPD3-A, and the characterization was not performed.

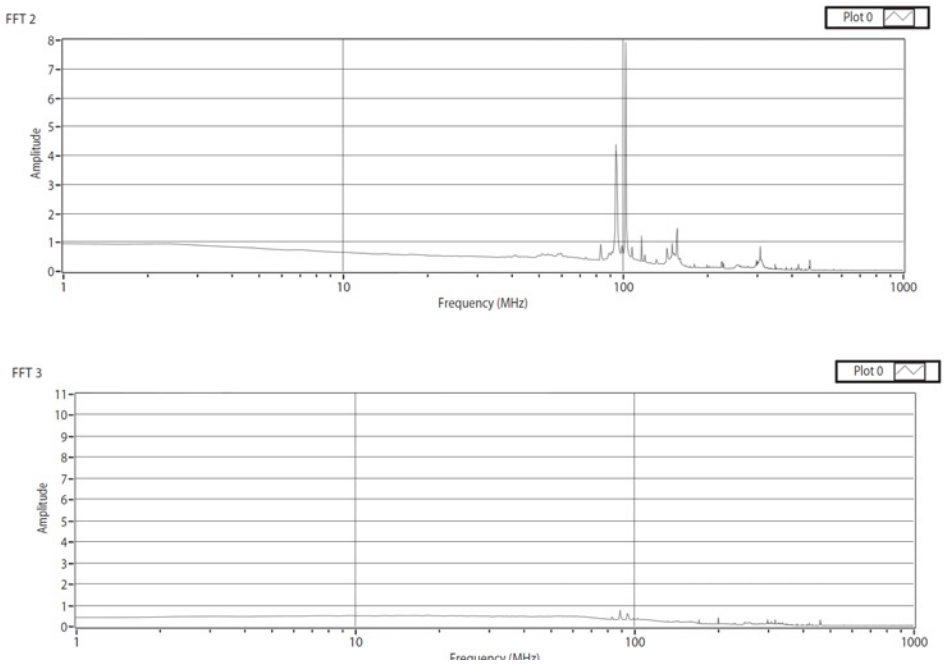

Figure 4.4: Noise in the system before and after the circuit within the LED-pulser was connected to the chassis of the pulser. This noise was not always present since moving the wires around a bit could result in connecting or disconnecting the circuit to ground accidently. The connection to ground is now stable. Noise histogram (a) without, and (b) with common ground.

4.1.2 Data Acquisition System (DAQ)

The DAQ system used for the measurements performed is based on a previous setup at the detectorlab. The system was previously used by Hege A. Erdal [1] in her master thesis, where she characterized different types of MAPD detectors. The setup has been modified somewhat in order to adapt it to the MAPD3-N. There are a few sections in which various equipment has been placed, and these will be referred to as the:

- Black box: Electrostatically shielded box, preventing unwanted electromagnetic interference or optical noise from reaching the sensitive parts of the measurement system.
- Device rack: This is a simple rack with various power supplies, measurement devices and a signal generator. A image of this rack can be seen in Figure 4.5, and a schematic view is given in Figure 4.6.
- NIM[2] rack: This rack contains various devices, but for this thesis only the fan-out and signal delay units will be used. The NIM rack can be seen in Figure 4.5.
- VME[3] rack: This rack contains the Analogue to Digital Converter (ADC) and a PCI[4] bridge, connected to a PCI-card in the PC, used for the read out of measurements. This rack can be seen in Figure 4.5

The chain of events during a normal measurement starts by the signal generator sending a NIM compatible trigger pulse to the fan-out device in the NIM-rack. The fan-out device then splits this signal, sending it to trigger input of the ADC (in the VME-rack) and to the trigger of the pulser (in the black box). This will ensure that the ADC is recording at the same time as the pulser sends out a light pulse to the MAPD. The pulser sends very short pulses of light through an optical fiber (either directly to the MAPD, or through a monochromator (see Section 4.1.2)). The MAPD will detect the signal and send it to the preamplifier, which amplifies the signal before sending it out of the black box and to the ADC. From the ADC the signal is sent via the PCI-module of the VME-rack, into the PC controlled by LabVIEW. LabVIEW reads out the sampled signal from the ADC and processes this along with data from the other instruments in the device rack, connected to the PC by USB or GPIB connectors.

Black box

The purpose of the black box itself has been explained in Section 4.1.1. This section will give a short description of the devices within the box, which contains:

- **LED-Pulser:** Provides the MAPD with a rapid light pulse (¡ 1 ns). Adjusting the supply voltage of the pulser will change the light yield of the

[2]Nuclear Instrumentation Module
[3]VersaModular Eurocard bus
[4]Peripheral Component Interconnect

Figure 4.5: The image to the left shows the device rack, while the image to the right shows the NIM rack (top) and the VME rack (bottom).

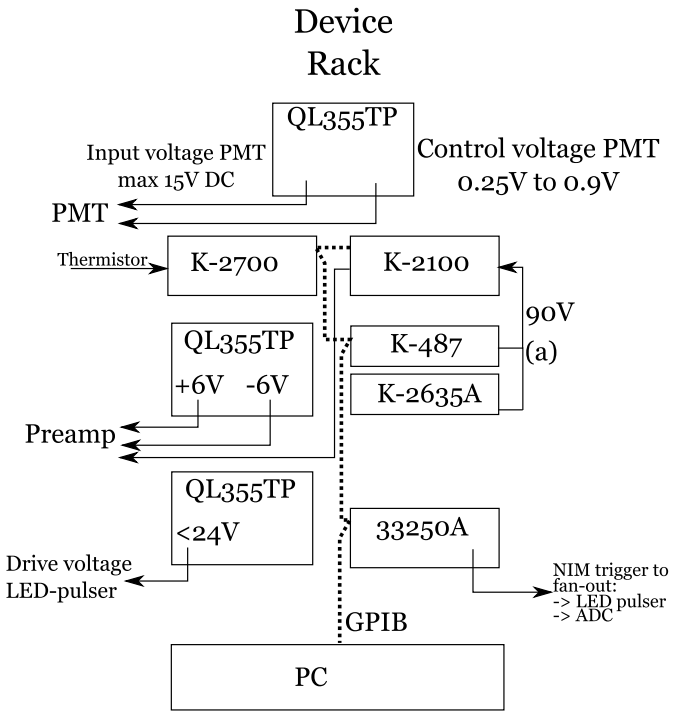

Figure 4.6: Schematic view of the device rack. The dotted line represents the GPIB connection from the PC to some of the instruments, connected in series. K-487 and K-2635A are both connected to K-2100. This connection simply allows the K-2100 to measure the bias voltage sent from these devices to the MAPD. Only one of the two are used at a time, but both are available due to practicalities.

Figure 4.7: The monochromator with a plastic adapter attached. The box connected on the right is the LED pulser, the black wire to the left is the fiberoptic cable.

LED, and in this way pulses with very little light, required for the absolute gain measurements, or a relatively high amounts of light for measurements such as the PDE can be provided. The pulser can either be connected directly to the MAPD via a fiberoptic cable, or via the monochromator.

- **Monochromator, Optometrics LLC, DMC1-02:** A monochromator for selection of narrow wavelengths of light. Light sent from the pulser enters the monochromator through a slit, is reflected by a folding mirror onto a spherical collimating/focusing mirror and is directed into a grating. The grating disperses the light and sends it back to the collimating/focusing mirror, before a portion of the light is reflected back onto a second folding mirror, and finally out through the slit at the output side of the monochromator. The size of the slits varies the resolution of the device. If the standard $300\mu m$ slits are replaced by 150 μm slits the resolution would be doubled, but the throughput of light would decrease by a factor 4. In this setup the standard 300 μm slits provided with the device were used. They were proven to give a sufficient amount of light and have a wavelength accuracy of $\pm$ $0.2nm$. The monochromator has a digital display, operated manually. The wavelength is displayed in nanometers with a readability of 0.2nm, with a supported range of wavelengths of 200-800nm, which covers the efficient spectrum of the MAPD3-N well. A mounting was made for the monochromator in order to attach the LED-pulser and a fiberoptic cable to the input and output of the device, respectively. The fiberoptic cable is splitted in two, making it possible to connect one end to the MAPD and one end to a reference detector such as a PMT. Pictures of this setup can be seen in Figure 4.7 and 4.8.

- **Preamplifier:** Fast, low-noise preamplifier with a gain of $\sim$197. Built and provided by the INR, Moscow.

- **Hamamatsu PMT, H6780-02:** A PMT used as a reference in PDE measurements with an adjustable gain from $\sim 10^2$ to $\sim 2 \cdot 10^6$.

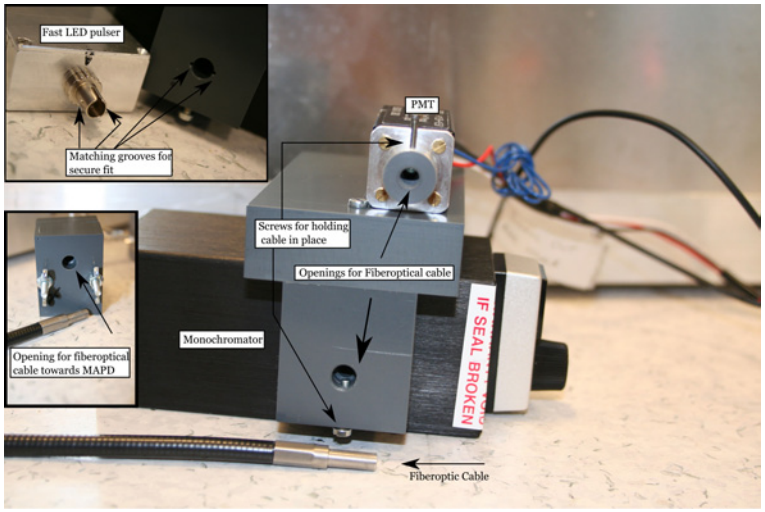

Figure 4.8: The mountings of the light system. The parts include the monochromator with an adapter, allowing the attachment of a fiberoptical cable and the LED pulser. The fiberoptical cable is connected to MAPD and PMT by custom adapters.

- **Thermistor:** A simple two-wire thermistor was used to measure the temperature of the MAPD during measurements where the measured parameter varies with the temperature of the detector. The thermistor is connected to a copper plate with approximate dimensions of 1,1x0,3x2,7cm^3. The copper plate has two holes for the MAPD connectors to pass through, inserted with plastic insulators in order to avoid short circuiting the two legs of the MAPD with the copper plate. This setup results in a good contact between the copper plate and the chassis of the MAPD, enabling the copper plate to function as a thermal buffer or stabilizer for the MAPD. Being in direct contact with the MAPD allows very accurate temperature measurements. The thermistor is calibrated and has a presicion of about 1/100°C.

Device Rack

Various devices used in the experiment have been placed in the device rack. The measurement devices in this rack are either connected to the PC by a GPIB connection, or a USB connection. A short listing of the devices in the device rack will be presented here.

- **TTi QL355TP Power supply**: Three of these are used in the setup. Each device has two outputs and supplies an accurate voltage to some of the devices in the setup. One power supply is used to power the PMT, one is used for the preamplifier and the third one is used to set the drive voltage of the LED-pulser.

- **Keithley 2700 multimeter/DAQ system**: Used for reading out the thermistors used in the experiment.
- **Keithley 2100 multimeter**: Primarily used in connection with a Keithley 487 picoamperemeter/voltage source. The K487 was previously used to set the bias voltage of the MAPDs, but did not display a satisfactory accuracy of the voltage it supplied. The K2100 was therefore used to precisely measure the voltage supplied from the K487 during measurements. The K2100 is still in use by some LabVIEW VIs to measure the bias voltage.
- **Keithley 2635A sourcemeter**: Used for providing the MAPD with bias voltage and measuring the current going through the MAPD, e.g. in the dark current measurements. This device gives a precise measurement of the supplied voltage, and can be used independently of the K2100.
- **33250A 80MHz function/arbitrary waveform generator**: Provides a NIM compatible trigger pulse for the LED pulser and the ADC.

ADC

The ADC used in the experiments is a CAEN Mod. V1729A. This is a 14bit ADC with a dynamical range of -1V to 1V, able to take 2 gigasamples per second. It samples the analogue signal continously at the sampling frequency and stores the values in a circular analogue buffer. The capacity of the buffer is 2560 samples, out of which 2520 are valid, corresponding to a measurement time of about 1000ns. The experiment only requires about 200ns, well below the capacity of the ADC. Each time the ADC is triggered it fills up the entire buffer before it can be read out, causing any trigger pulses received while the ADC is recording to be ignored. The ADC is the slowest part of the system, and in order to provide higher statistics within a reasonable measurement time, a faster ADC would be required.
The readout for the equipment in use have been done by LabVIEW. The various programs, known as Virtual Instruments (or VIs), will be discussed in the section describing the specific measurement for which the VI was used.

4.1.3 Improved setup for reproducability and stability of measurements

In order to increase the reproducability and to be ensure that the various devices in the setup are properly aligned, e.g. that the fiberoptic cable points directly at the MAPD, some simple parts were made customly for the setup. These parts have been partially designed in AutoCAD[5], before discussing practical aspects of the design and creation with Roald Langøen (staff engineer at the mechanical workshop at the Department of Physics and Technology), who then produced the components. In order to keep the MAPD aligned with the fiberoptic cable and to ensure a good contact to the copper plate of the thermistor, a set of three plastic pieces is being used (see Figure 4.9). the MAPD is fastened to the thermistor

[5]AutoCAD is a Computer Aided Design/Drafting software made by Autodesk

by pushing part 1 and 2 together, the third part can be one of two end pieces designed for two different types of available fiberoptic cables. The three pieces are aligned and tightened by two bolts and nuts. In addition a similar alignment setup was made for the monochromator, in order to have a stable mounting for the fast LED-pulser and the fiberoptical cable out of the monochromator. The fiberoptical cable can be tightened by a screw in order to lock it in place. This is especially important for measurements such as the PDE, where the results will not be valid if the fiberoptical cable is moved even slightly. This will be discussed further in section 4.2.4

4.2 Measurements

There are several parameters of the MAPD that are interesting to know when working with these detectors. When using MAPDs for measurements it is vital to know how high the gain is, i.e. what output signal can be expected for a given amount of incident light. It is not, however, certain that all the light incident on the detector will create a signal, making it important to know the probability of an incident photon to produce a detection event (see Section 2.7.4 about the PDE). Since the PDE depends on the wavelength of the incident light it can be extremely useful to know which wavelengths that yields the optimal results. Having this knowledge allows for applying proper wavelength shifters to either the scintillators directly, or by using wavelength shifing fibers, matching the wavelength of the light to the spectral response of the MAPD. Varying the bias voltage of the device will also change the gain, but at the same time it will have an effect on the noise of the detector. Knowledge of how the various parameters vary with the voltage thus allows the user to select an optimal bias voltage, where the gain/noise ratio is at a maximum.

4.2.1 Dark Current

The dark current, i.e. the current going through the MAPD when no incident light is present, was measured by a sourcemeter[6]. The sourcemeter provides the MAPD with a stable bias voltage, and measures the current going through the MAPD with high precision. A diagram of the setup can be seen in Figure 4.10. A LabVIEW program, dark_current.vi, has been used to control the sourcemeter during the measurements, both for setting the bias voltage and recording the currents measured. The dark current depends on the bias voltage, and therefore the measurement series were taken over a range of voltages from 89.0 V to 91.2 V. The measurements were taken in 42 steps over the range. The first measurement is done at 0 V in order to have a reference of the background noise and when no bias voltage is applied, with the results deducted from the following measurements when a bias voltage was applied.

[6]Keithley 2635A Sourcemeter

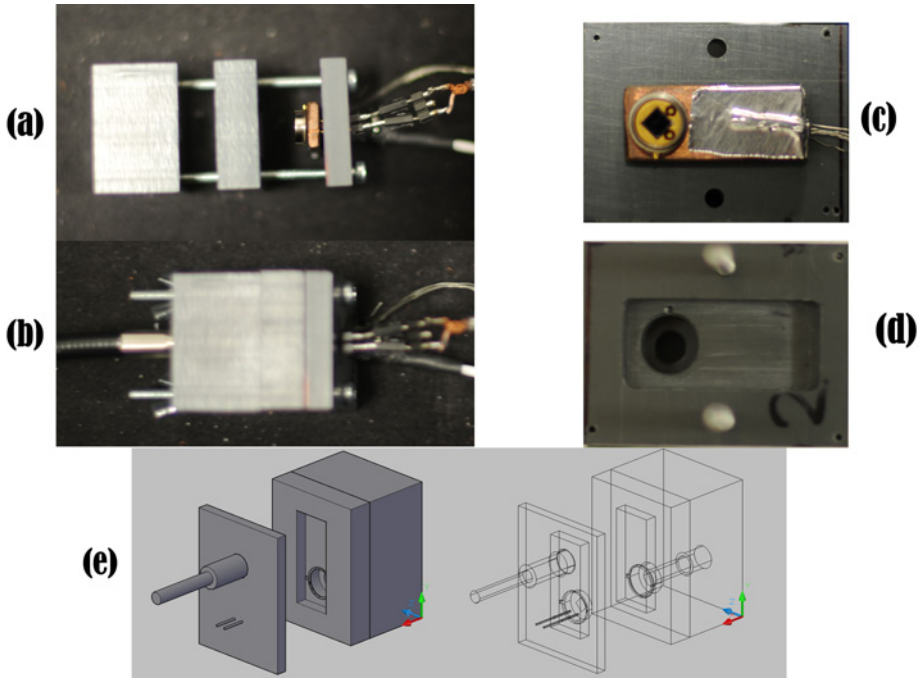

Figure 4.9: Plastic casing for securing the thermistor, MAPD and fiberoptical cable in place, for increased repeatability of measurements and improved alignment of the components. (a and b): The piece for the optical connector is shown to the left, the thermistor and MAPD are attached to the right part, which locks into position with the middle part. (c and d): (c) shows the MAPD connected to the thermistor. To the right in the image thin metal wires can be seen. These connect the copper plate of the thermistor to ground. (d) shows the grooves which matches the MAPD and thermistor. The third plastic piece can be seen through the hole in the middle, which is where the optical fiber will enter. This hole is aligned with the face of the MAPD. (e): Schematic view of the parts from AutoCAD made while planning the design. The pins of the MAPD and the thermistor cable can seen emerging to the left.

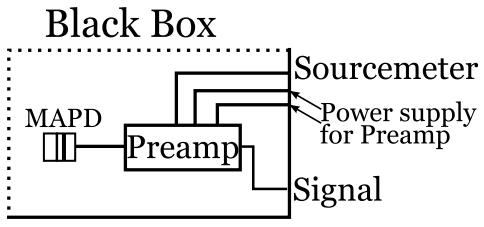

Figure 4.10: Simple model of the dark current setup. There is no light shining on the MAPD. The sourcemeter provides the bias voltage and reads out the current through the MAPD.

4.2.2 Absolute gain

The gain of the MAPD has been measured in respect to the temperature and bias voltage in this thesis. This section will describe the process of determining the gain at a single state, i.e. with no variations in gain or temperature, in order to establish the basic setup for the measurements where variables are changed. This setup relies on the few photoelectron peaks for determining the gain of the detector[7]. When a single pixel of the detector is fired it will result in a signal with a given amplitude. If two pixels are fired this signal will have an amplitude twice the size of that which a single pixel yields (see Section 4.2.2). This pattern makes it possible to calculate the gain by determining the average distance between the peaks given by an increasing number of fired pixels. An example of such a pattern can be seen in Figure 4.11. There are 5 easily distinguishable peaks in the figure. In addition to the photoelectron peaks there will normally be a *pedestal peak* as well, representing the situation where no pixels are triggered, and it is thus the first peak to appear in the histogram. The distance between the pedestal peak and the first photoelectron peak will be the same as the distance between any other two neighbouring peaks, meaning that the pedestal peak can be included when calculating the average distance between the peaks. In the lower half of Figure 4.11 the first four peaks have Gaussian fits applied to them. The values of this distribution is used to determine where the center of the peak can be found, and it also provides the uncertainty of a given peak. The absolute gain of the MAPD is given as:

$$G = \frac{\overline{D}}{G_{preamp} \cdot q_e}, \tag{4.1}$$

where $\overline{D}$ is the average distance between the photoelectron peaks, G_{preamp} is the gain of the preamplifier and q_e is the electron charge.

Gain vs. Bias voltage

The gain of the MAPD varies with the bias voltage, and in order to find the dependence of the bias voltage a set of gain measurements were performed in the range of 89.2 V to 90.9 V in steps of 0.1 V. These measurements were repeated for each of the four MAPD3-N samples in order to observe any variations from sample to sample. The LabVIEW VI used is similar to the one used in the measurement of the absolute gain for a single bias voltage, but has an implemented function for setting the bias voltages and storing the measurements for each bias voltage into a separate file.

Gain vs. Temperature

The gain MAPDs depends on the temperature of the device. If the detectors are being used in enviroments that do not have a stable temperature, this may

[7] Another method that can be used is to look at the Fourier transformed charge distribution. The photoelectron peaks will appear with a certain frequency which will then appear as a peak in the Fourier transformation. This peak can then be used to calculate the gain.

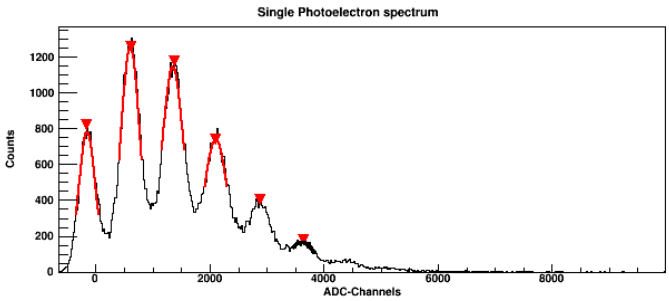

Figure 4.11: Histogram showing a few p.e. peaks from a gain measurement. The data is taken at 90.10 V, for MAPD3-N sample #24. The x-axis is represented as ADC channels, which will be transformed to represent the charge signal from the MAPD. The number of counts is displayed on the y-axis.

have an effect on the results obtained. Knowing the temperature dependence of the detector can help correcting for variations of the gain due to shifts in the temperature, or in order to estimate an uncertainty related to temperature variations. In order to measure the gain versus the temperature of the system, the same basic setup as used for the absolute gain measurements (Section 4.2.2) was taken in use. The main difference in the setup was the introduction of a system for adjusting the temperature. A simple solution was chosen, where two 0,5 liter bottles of water and one thermal element from a cooling bag were frozen in a standard household freezer (this approach has also been used in the setup previously [1]). After these were frozen solid they were wrapped in paper towels to absorb any condensed water that would be formed around the elements. A protective metal casing was put around the MAPD-holder before the bottles were placed on each side of the MAPD, and the cooling bag element was placed on top (see Figure 4.12. The temperature was observed to drop rapidly when the cooling elements were in place. This posed a potential problem with the measurements as there would not be a sufficient number of measurements to determine the few photoelectron peaks accurately for small changes in temperature. If the temperature changes quickly there will be a limitation to how many measurements can be taken in short steps of temperatures. To avoid this problem it was chosen that the measurements should instead be taken at rising temperatures. The setup was allowed to cool down to a minimum, where the temperature seemed to stabilize, before the measurements were started. The system then performed measurements over $\sim$ 10 hours where the temperature slowly rised from $\sim$ 13.5°C to $\sim$ 24.0°C. The LabVIEW VI was slightly altered from the one in the absolute gain measurements, making it run in an infinite loop where it would take a set of one million measurements, store the measurements and start over again. This was done to allow the setup to run by itself during the night.

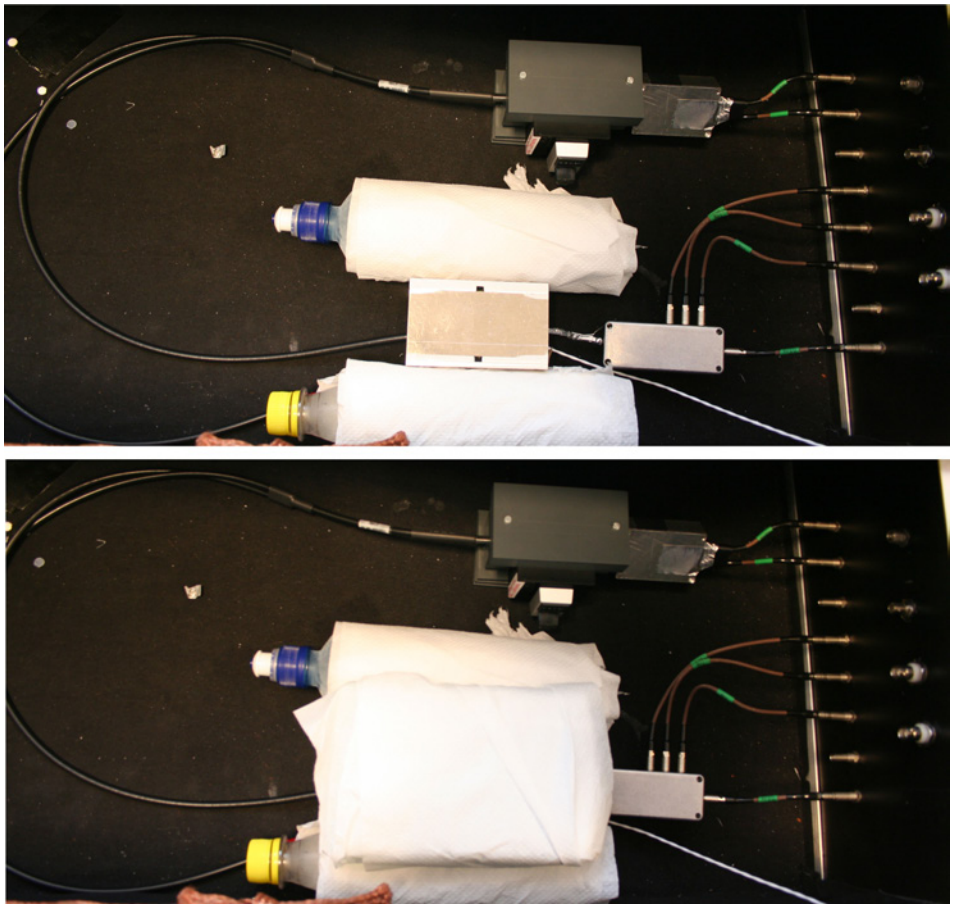

Figure 4.12: A picture showing the position of the cooling elements within the blackbox. In the upper part, a U-shaped metal container with open ends has been placed over the MAPD-holder, making it safer to place the cooling element on top of the detector, without having to worry about condensed water dripping onto the MAPD. In the lower part all three cooling elements are in place.

4.2.3 Dark Rate

The dark rate is the main source of noise for a MAPD, making it interesting to study this variable. The experimental setup used for measuring the gain of the MAPD can also be used in order to determine the dark rate. In order to do this the LED-pulser is turned off, providing a dark enviroment for the MAPD. The ADC is then set to read out the signal from the MAPD and every time the signal exceeds a threshold value set to half the amplitude of the first photo electron peak (found in the gain measurements), the pulse heigth is stored. From these measurements the dark rate can then be determined.

While the dark rate measurements have been performed successfully for MPPCs at the detector lab in Bergen before, the dark rate for the MAPD3-N can not be determined successfully. The threshold value of half the amplitude of the first *p.e.* peak lies very close to the average noise level of the system, causing the noise to trigger events that can not be distinguished from dark rate events. Attempts were made using an alternative approach where the threshold was set to 1.5 of the first p.e. peak, but the noise of the system still represented a large part of the triggered events. As a result the dark rate can not be measured by the setup as it is at the current time, and further improvements to improve the signal to noise ratio must be made if such measurements are desired.

4.2.4 Photon Detection Efficiency

The PDE measurements will determine the spectral response of the MAPD, i.e. how well it detects light of various wavelengths. A narrow range of wavelengths can be selected by the monochromator from a wider range of wavelengths sent into it. In order to provide a wide selection of specific wavelengths the light source need to be able to provide these. When using a LED as the light source the range of wavelengths is very limited since a normal LED will only have a narrow distribution around its peak wavelengths, resulting in a range of about 10nanometers. In order to provide a large range of wavelengths this means that one has to use several LEDs of varying peak wavelengths in order to provide a good spectrum. In this experiment a white LED was used to provide measurements in between these values. A white LED provides a wide spectrum of wavelengths, but the intensity of each wavelength varies a lot. An example of the light yield of a similar white LED is shown in Figure 4.13. At wavelengths where the yield is low, compensation had to be made by measuring more events for the given wavelength, increasing the voltage supplied to the LED in order to get a higher output, or by using a longer pulse of light. The LED-pulser used for the gain measurements has a limitation to its input voltage, and increasing the voltage past this point will cause it to trigger randomly and thus give out pulses independently of the common trigger sent to the pulser and ADC. This prevented the luminosity of the LED to be increased to the levels needed for the PDE measurements. During the gain measurements the wavelength of light sent through the monochromator was selected to be the peak wavelength of the LED in the fast-pulser. While scanning through a large range of wavelengths most of the measurements are taken at wavelengths which have a much lower luminosity than the peak, making it nessecary to increase the LED

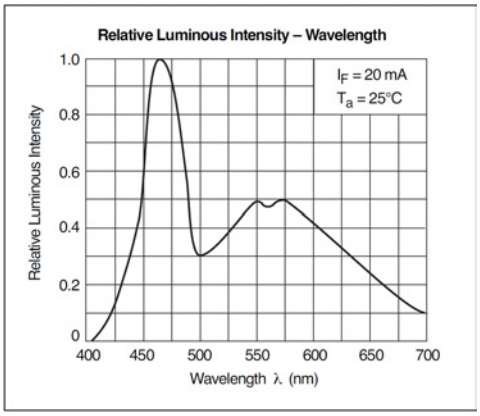

Figure 4.13: Relative luminous intensity at different wavelengths of a white LED.

voltage beyond the limits of the fast pulser, and thus an alternative approach was needed. By connecting the LED directly to the signal generator the voltage can be increased, providing more light for the measurements. The pulse width can also be regulated allowing for longer pulses of light, meaning that more light will hit the detectors for each measurement. This may potentially cause more photons to hit a single pixel, but as the light of the LED was still relatively low for most wavelengths this is not considered to have a large effect on the measurements. The detected signals were at all times kept well below the limits of the dynamical range, either by not having more light available or by adjusting the supply voltage or pulse time of the LED. From the monochromator a splitted fiberoptic cable was used to send approximately half of the light to a PMT and half of the light to the MAPD. An image displaying the splitting of the light through the fiber can be seen in Figure 4.14. The PMT functions as a reference detector since its spectral response is given by the company producing them (Hamamatsu). The specifications for the radiant sensitivity of the PMT cathode can be found in Appendix B. In this section the quantum efficiency has also been calculated, and is presented in Figure 4.15. The results for the PMT can thus be weighted in respect to the quantum efficiency curve, and the quantum efficiency of the MAPD can thus be determined. In order to calculate the quantum efficiency of the PMT, a set of values were read out from Figure B.1. The values were read for wavelengths between 425-700 nm, in steps of 5 nm, corresponding to the highest measurement density that was performed. The radiant sensitivity of the cathode is given in mA/W. In order to convert this to the quantum efficiency the following formula was used:

$$QE = S \cdot \frac{\frac{ch}{\lambda}}{e}, \tag{4.2}$$

where e is the elementary charge, c is the velocity of light in vacuum, h is plancks constant, S is the cathode radiant sensitivity and λ is the wavelength which the QE will be calculated for. The formula gives the quantum efficiency as a number

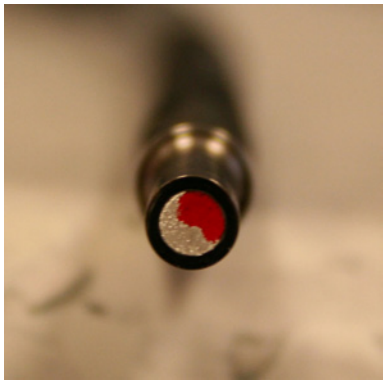

Figure 4.14: Illustration of how the fiberoptical cable splits the light into the two ends. In order to see the split, one end was pointed at a red object, while the other end was pointed towards a bright white surface. The cable can either be used with one input and two outputs, or alternatively with two inputs and one output, e.g. if two pulsers were to be connected to one MAPD in order to test the recovery time of the detector.

of electron-hole pairs produced per incident photon. The energy of the photons vary with its wavelenght, and since the cathode sensitivity is given in watts the wavelength must be taken into account. A plot of the quantum efficiencies used in the calculation of the QE for the MAPD3-N can be seen in Figure 4.15. While an absolute value of the quantum efficiency for the MAPD is desirable, it is not possible to obtain with the current setup. There are many uncertainties involved in the system which prevents this value from being determined:

- The light yield of the LED is not high enough for all the wavelengths in the desired range. The detectors should be illuminated enough to give a good signal, but still be kept within the linear response range of the MAPD, i.e. saturation by multiple photons hitting one pixel per detection period should be avoided.

- The fiberoptical cable is splitted, and it is difficult to know how high the fraction of light will be at each end of the cable. An illustration of the splitting of light can be seen in Figure 4.14. This can be compensated for by having two equal reference detectors, e.g. PMTs, and measuring the difference of the light in each end, thus yielding a fraction of the output for each end. The stabilization of the cables have been made possible by being able to lock the cable in position for both the PMT (Figure 4.8) and for the monochromator (Figure 4.7).

- Despite the locking of the fiberoptical cables, the dispersion of light out of the cables causes another problem. If the distance between the cables and the detectors, e.g. the PMT and MAPD, are not exactly the same, the concentration of light will vary. Testing the fraction of light for each end

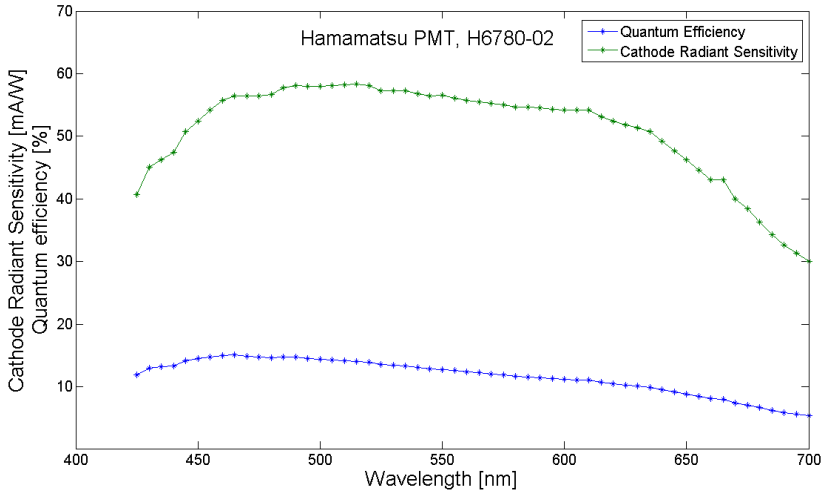

Figure 4.15: Cathode radiant sensitivity and quantum efficiency of the Hamamatsu PMT, H6780-02.

of the cable may then not be valid if the adapter is changed from the PMT adapter to the MAPD adapter. With the current setup this distance is not precise enough.

- The sensitive areas of the PMT and the MAPD in use are not the same. If a given, exactly equal amount of photons are sent through each end of the fiber, an uneven amount of photons can hit the sensitive areas of the two detectors. There will be a dispersion when the photons exit the cable, and the photons are more likely to miss the detector with the lesser sensitive area. The MAPD has an active area of 3x3mm^2 while the PMT has a circular active area with a radius of 4mm, yielding an area of 4x4xπ mm^2. This represents a difference in size of factor ~ 5.

These and other potential problems limit the possibility of finding the absolute value of the quantum efficiency for the MAPD. Instead a compromize has been made

4.2.5 LabVIEW - Control of Measurements

LabVIEW[8] is a visual programming language produced by National Instruments. The program allows the user to make *virtual instruments* (VIs), that enables a wide range of possibilities for data taking, processing, storing and display. In the setup used in this thesis, all the data taking has been done via a variety of LabVIEW VIs. A basic VI consists of initializing the instruments in use, setting

[8]Laboratory Virtual Instrumentation Engineering Workbench.

the required parameters before the measurements starts (or during measurements if a variable is to be changed), starting the measurement cycle, obtain data via instruments such as multimeters or the ADC, process the data and finally store the data to a file and present it visually. The visualisation is mostly used as an indicator to control if everything seems to be performing as it should. After a measurement the data will then be processed further and presented by other tools. A combination of ROOT[9], Python and Matlab have been used for the processing and presentation of data.

[9] http://root.cern.ch/

Chapter 5

Results

5.1 Results

5.1.1 Gain vs. Bias Voltage

The measurements for the gain versus the applied bias voltage is shown in Figure 5.1. From the figure it can be seen that the gain increases quite linear while increasing the bias. For some of the measurements the MAPD broke down while increasing the bias, making it difficult to determine the gain. A series of measurement for the #174 sample can be seen in Figure 5.2. As the bias voltage $\sim$ 90.5 V the peaks are becoming less defined, and around $\sim$ 90.7 V they can no longer be determined for this sample. For sample #24 and #16 peaks could be distinguished up to 90.9 V, for sample #5 the peaks could not be observed for voltages above 90.7 V. It can be seen from Figure 5.1 that the gain of sample #5 and #174 is higher than for the last two samples, which is likely to be the reason for their earlier breakdown. It seems that the detectors break down when they reach a gain of $\sim$8.2 - 8.6$\cdot 10^4$. The gain was only measured for 4 samples, and a larger set of samples would be valuable in order to determine how high the variation in the characteristics are. The variations of the temperature will be discussed in the following section. The results from the gain vs bias voltage measurements can be seen in Table 5.1. These values are obtained from the plot

Table 5.1: The gain of 4 different MAPD3-N samples

Sample nr.	Gain	%Vdep	Cpixel	Vbd
5	56764	5.43005	4.93E-15	88.1584
16	54880	5.22733	4.59E-15	88.087
24	54240	5.55342	4.82E-15	88.1993
174	65250	4.72405	4.94E-15	87.8832

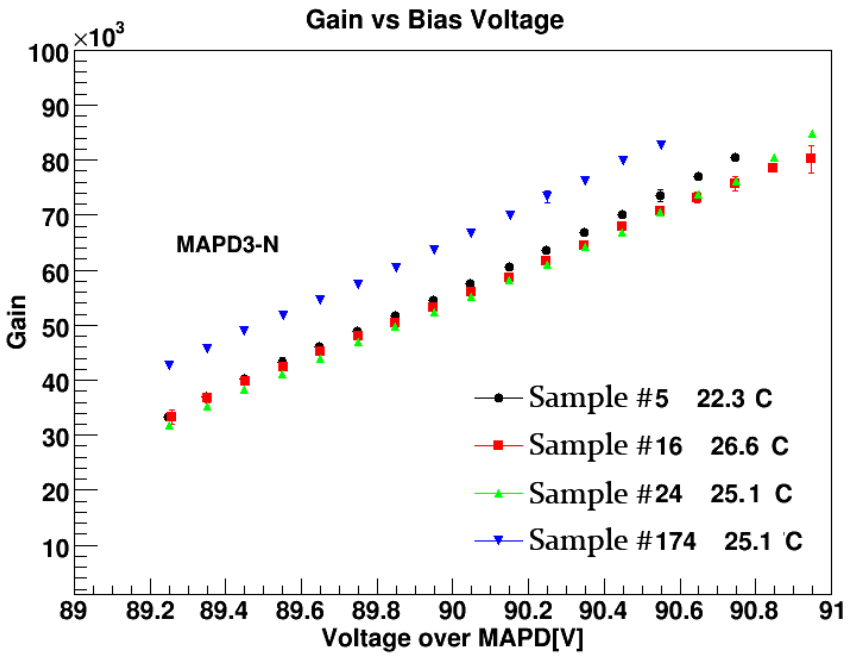

Figure 5.1: The measured gain of a MAPD3-N at increasing bias voltages for 4 different samples.

in Figure 5.1. As expected from Equation 2.24;

$$G = \frac{Q}{q_e} = \frac{C(V_{bias} - V_{breakdown})}{q_e}, \tag{5.1}$$

the gain shows a linear dependence. By using a linear fit to each curve, we find a line in the form of:

$$G(V) = aV + b, \tag{5.2}$$

where a is the increase in gain if the voltage is increased by 1. The pixel capacitance C_{pixel} and the breakdown voltage $V_{breakdown}$[1] can be obtained from:

$$C_{pixel} = a \cdot e, \tag{5.3}$$

and:

$$V_{breakdown} = -\frac{b}{a}. \tag{5.4}$$

[1]The breakdown of the detector has previously been mentioned as the point where the detector stops giving a linear response. This breakdown voltage, however, refers to the minimum breakdown voltage.

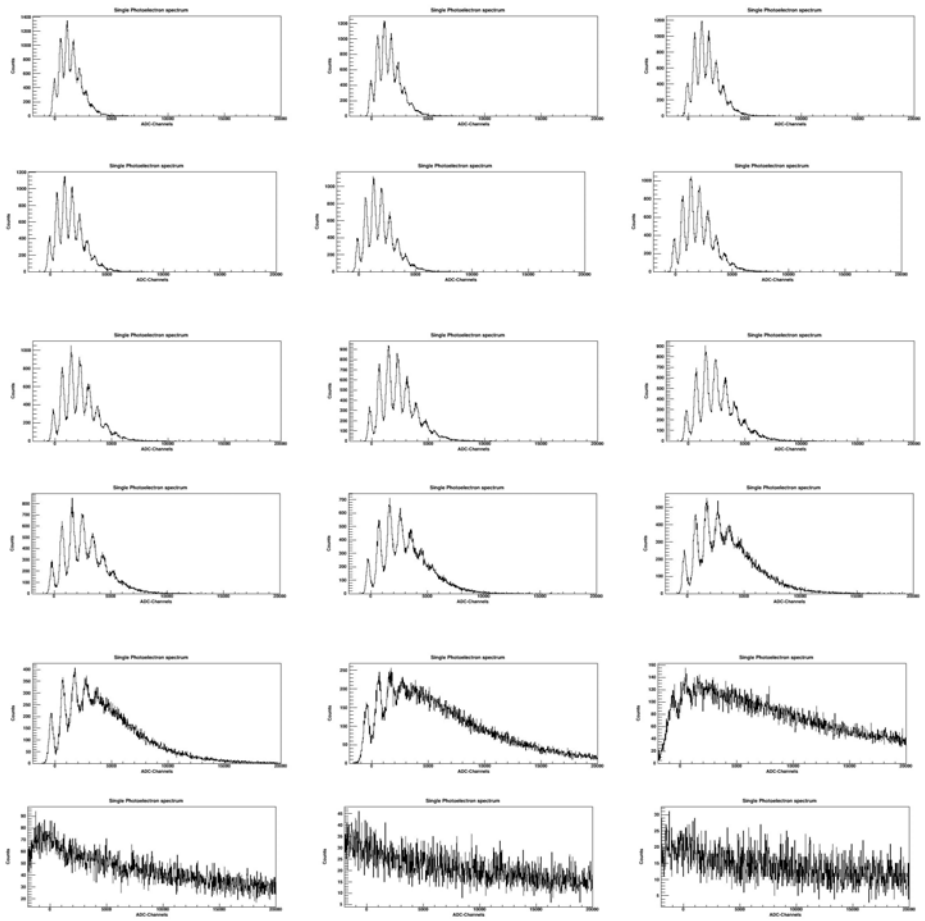

Figure 5.2: A measurement serie for the #174 sample, showing the photoelectron peaks detected at various voltages. The top left figure is a measurement taken at 89.20 V, and each of the histograms following to the right and continuing on the next rows displays the peaks with increments of 0.1 V. The y-axis represents the number of counts for a given ADC-channel (x-axis). Note: The histogram in the top left corner has a y-axis limited to 1400 counts. As the gain is increased the peaks are less defined and the histogram is smudged out. This results in a lower number of counts per channel, and for the 90.9 V histogram the y-axis has a maximum of only 31 counts.

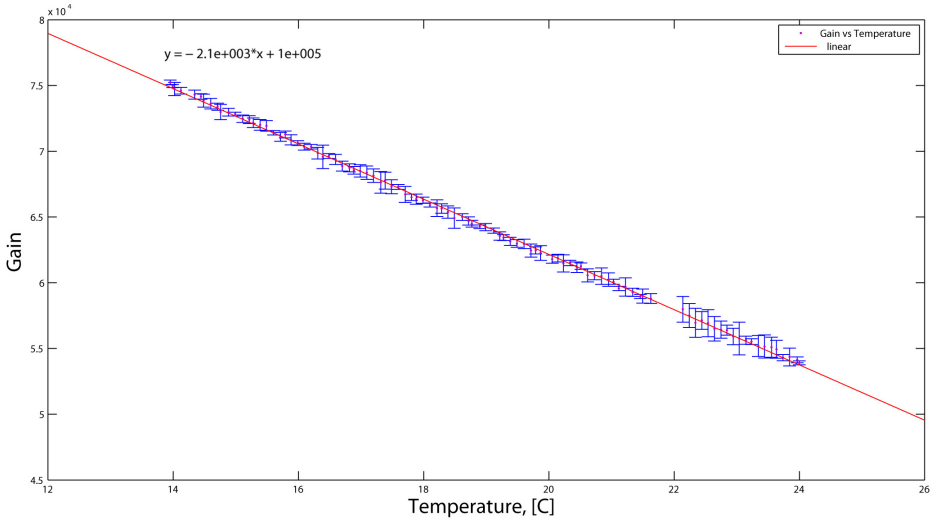

Figure 5.3: The measured gain of a MAPD3-N at increasing temperatures.

5.1.2 Gain vs. Temperature

The temperature dependence of the MAPD3-N detector was measured in a range of temperatures from $\sim$ 13.5°C to $\sim$ 24.0°C in steps of 0.1°C. The results from such a measurement is shown in Figure 5.3. By applying a linear fit to the measurement points, a decrease in gain of $2.1 \cdot 10^3$ per °C was found. A small gap in the temperatures can be seen around 21.6 - 22.0 °C. This is caused by the cooling elements being removed, causing a short pause in the measurements. The following measurements drop somewhat in accuracy as the temperature started increasing more rapidly after this removal.

This result can be used in order to estimate values of the gain at different temperatures by using the gain measurements taken in the previous section. In Figure 5.4 the gain measured for each given bias voltage has been adjusted by the following equation:

$$G_{corr} = G_{meas} - (T - T_{ref}) \cdot 2100\ {}^{\circ}C^{-1}, \tag{5.5}$$

where G_{corr} is the corrected value of the gain, G_{meas} the gain measured at the temperature, T, and T_{est} is the temperature for which the gain is being estimated. The factor 2100 °C^{-1} corresponds to the decrease in gain for every °C the temperature increases, found by the linear fit in Figure 5.3. Figure 5.4 shows the estimated gain for some temperatures.

5.1.3 Dark Current

The dark current of each MAPD3-N sample was measured for increasing bias voltages, in 42 steps from 89.0 V to 91.2 V, and can be seen in Figure 5.5. The rise of the dark current is nearly linear with increasing bias voltages up to a certain

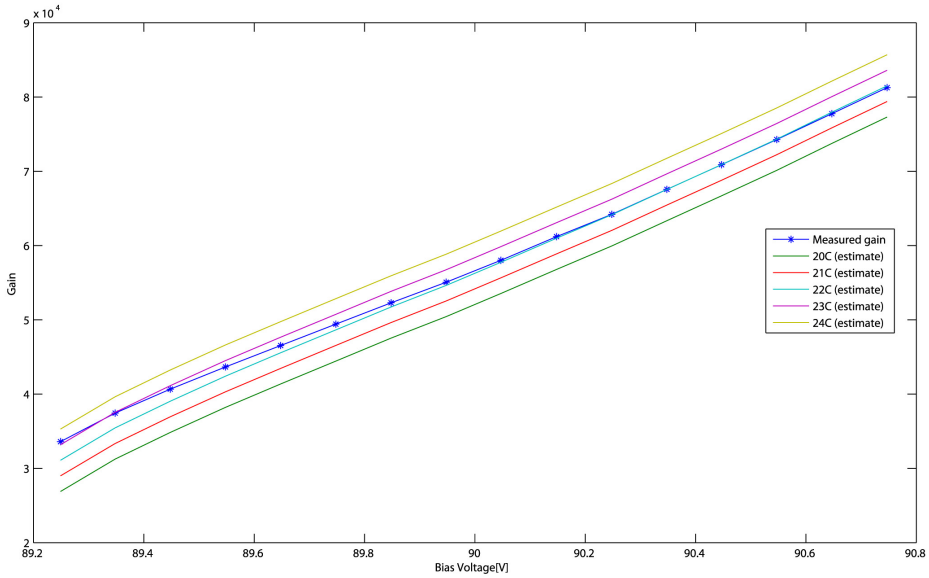

Figure 5.4: The measured gain for sample #5 at different bias voltages compared to the estimated gain at various temperatures. The measured curve has been measured under a variation of about 1 $°C$, corresponding to a change in gain of $\sim 2.1 \cdot 10^3$. A change in temperature of 1 $°C$ thus poses a relatively large uncertainty for the gain measurements, and should be taken into consideration while performing these calculations.

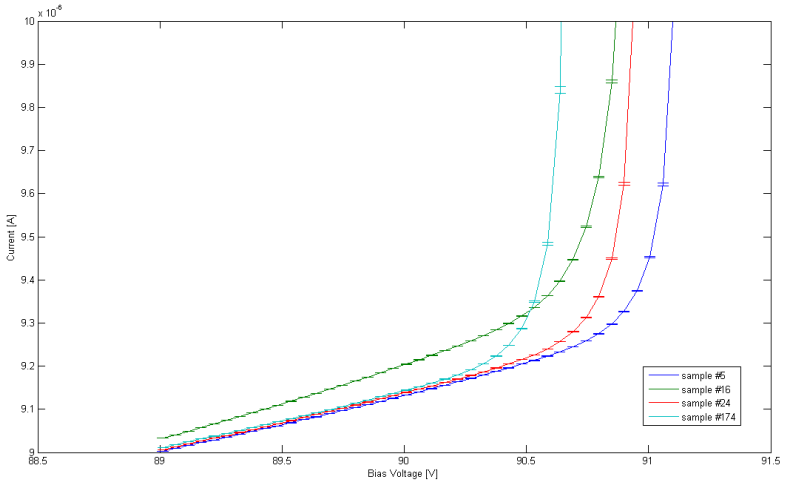

Figure 5.5: The dark current for all four samples of the MAPD3-N

Table 5.2: The dark current for all 4 MAPD3-N samples

Sample nr.	Dark current at 90 V [μA]	Increase for +0.1 V [μA]	Valid up to [V]
5	9.6	0.014	$\sim$ 90.6
16	9.3	0.018	$\sim$ 90.4
24	9.4	0.014	$\sim$ 90.4
174	8.9	0.013	$\sim$ 90.2

point, after which it increases rapidly. This point seem to correspond well with the bias voltage causing a breakdown in the gain vs bias measurements for all the samples. Sample #174 reaches this point before the other detectors in both the dark current and gain measurements, indicating that the properties of this specific sample deviates slightly from the other samples. See Figure 5.5 Table 5.2 shows the increase in dark current per increment of 0.1 Vf or each MAPD3-N sample, in the region where the increase is linear.

5.1.4 Photon Detection Efficiency

The photon detection efficiency was measured by comparing the output of a MAPD and a PMT while sending light from a white LED through a monochromator and onto the detectors via a fiberoptical cable. The PMT can be used as a reference detector in the measurements, as the spectral dependency of the cathode sensitivity is given by Hamamatsu (see Appendix B). The quantum efficiency for the MAPD

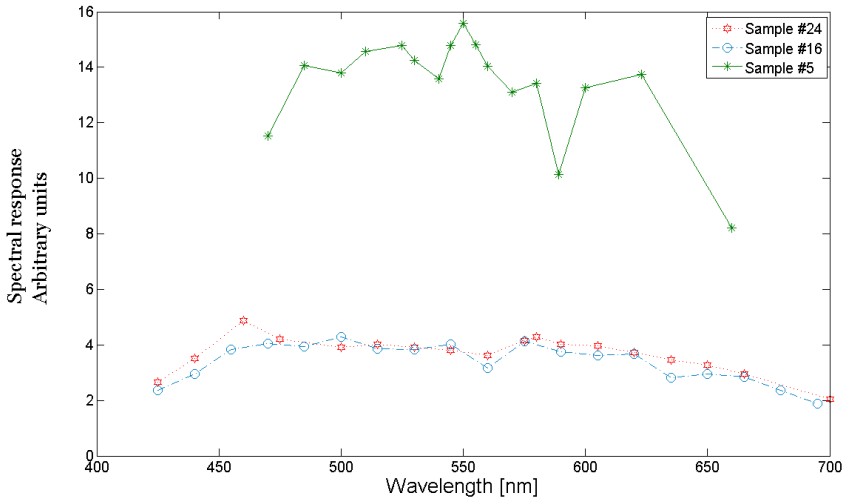

Figure 5.6: Spectral response of MAPD3-N samples 5, 16 and 24 in arbitrary units.

can be found by the following equation:

$$\frac{P_{PMT}}{QE_{PMT}} = \frac{P_{MAPD}}{QE_{MAPD}} \Rightarrow QE_{MAPD} = \frac{P_{MAPD} \cdot QE_{PMT}}{P_{PMT}}, \tag{5.6}$$

where P_{PMT} and P_{MAPD} is the number of photons detected by the PMT and MAPD, respectively, during the measurement at one wavelength, QE_{PMT} and QE_{MAPD} is the quantum efficiency of the two detectors. The PMT has a relatively stable gain for the variation in temperature of a few $°C$ which can be expected during a measurement series in the current setting. For the MAPD, however, a change by a few $°C$ can cause a large variation in the gain. This variation was compensated for by adjusting the total charge of the MAPD at each wavelength according to the results found in the gain versus temperature measurements (see Section 4.2.2)

In Figure 5.6 the spectral response for the MAPD can be seen, presented in arbitrary units. In Figure 5.7, the first figure, there are two parts. The upper part shows the number of photons detected by the PMT and the MAPD, while the lower part shows the quantum efficiency for the MAPD. The calculations performed in order to obtain these plots are obtained by first finding the number of photons detected for each detector: The results from the measurement series for one of the MAPDs can be seen in Figure 5.7. The figure is divided in two parts, where the upper part displays the number of photons detected by the PMT and MAPD for a given wavelength, and the lower part shows the quantum efficiency plotted against the wavelength of the incident light. In order to calculate the number of photons detected, the following equations has been used, for the PMT and the

MAPD, respectively:

$$P_{PMT} = \frac{CH}{8191 \cdot \frac{1}{n} \cdot G_{PMT} \cdot e \cdot R}, \tag{5.7}$$

and:

$$P_{MAPD} = \frac{CH}{8191 \cdot \frac{1}{n} \cdot G_{MAPD} \cdot G_{preamp} \cdot e \cdot R}. \tag{5.8}$$

CH is the sum of the signal read from the ADC for each wavelength, 8191 is the number of channels in the ADC, $\frac{1}{n}$ is a conversion factor from nanoseconds to seconds, due to the timing parameter of the ADC, G_{PMT} and G_{MAPD} is the gain for the PMT and the MAPD, G_{preamp} is the gain of the preamplifier of the MAPD and R is the resistance over which the signals have been read out. After having the number of photons detected, Equation 5.6 is used in order to find the quantum efficiency of the MAPD. This is the value plotted in the lower part of Figure 5.7. As a comparison, a similar curve measured at GSI has been included in Figure 5.8. The quantum efficiency in Figure 5.7 has been scaled up by a factor $\frac{4 \cdot \pi^2}{3x3}$, corresponding to the ratio between the areas of the sensitive volume of the PMT and the MAPD, as mentioned in Section 4.2.4

The process of the data taking has been done by a few different methods. The first attempt was to use the fast LED-pulser as the light source, sending short, fast pulses towards both of the detectors. This method gave very small amounts of light to the detectors, and for some wavelengths the signs of few photoelectron peaks were starting to show, and therefore it was concluded that this was not an optimal solution for the measurements. During PDE measurements it is desired to have a relatively high intensity of light, while still avoid reaching the saturation effects that occur when more than one photon hits a single pixel before the pixel has recovered from the previous breakdown. In order to increase the light yield, the next attempt was to connect a LED directly to a signal generator. Since the LED pulser had an upper limit to the supplied voltage for the LED, connecting the LED to the signal generator allowed higher voltages to be sent to the LED. In turn this provided a higher intensity of light towards the detectors. Due to the variations in the luminosity of the LED for different wavelengths, the light yield was still too low for a wide range of wavelengths. In order to compensate for this, the pulse length was increased, causing more light to be emitted towards the detector per pulse. The pulse length was kept in the range between 30-70 ns for the last measurements, including the one in Figure 5.7. One drawback of increasing the pulse width it the increased possibility of two or more photons hitting the same pixel before it has recharged, potentially lowering the number of detected events. A decrease in the quantum efficiency of a factor ~ 3 was observed after changing from the fast pulser to the signal generator (see Figure 5.6), which might indicate that more photons have hit the same pixel, decreasing the number of detected photons. For sample #174, both the number of detected photons and the quatum efficiency is plotted. It can be seen that the two curves in the upper plot follows the same pattern, matching the curve shown in Figure 4.13 quite well. Note should be taken, however, that the light yield was lowered for the most intense wavelengths, in order to avoid saturation, and increased for the

weaker wavelengths. There were still notable differences in the intensity though, as a perfect normalization of the light could not be acheived, due to limitations to the pulse length and voltage supplied to the LED.

. The plot corresponds fairly well with the plot in Figure 5.8, and has a similar quantum efficiency and form of the curve. The curve obtained for sample #174 has a somewhat broader maximum however. It is important to keep in mind the uncertainties mentioned in Section 4.2.4 when studying this plot. The maximum of the quantum efficiency stretches over a range from about 460 nm to 600 nm.

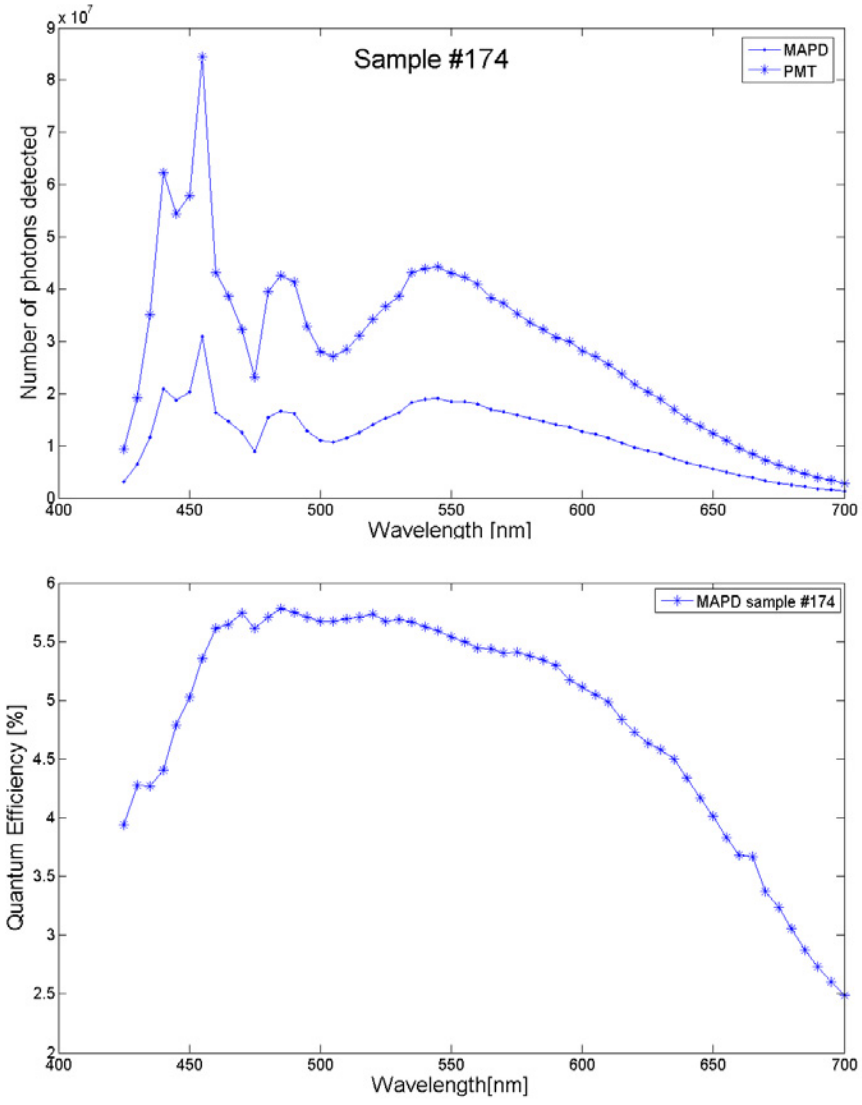

Figure 5.7: Measurements of the (upper): Number of photons detected by a PMT and MAPD sample #174 for various wavelengths, and (lower): The quantum efficiency of MAPD3-N sample #174. The quantum efficiency has been scaled by the ratio between the area of the sensitive area of the PMT and the MAPD, which is ~ 5.6.

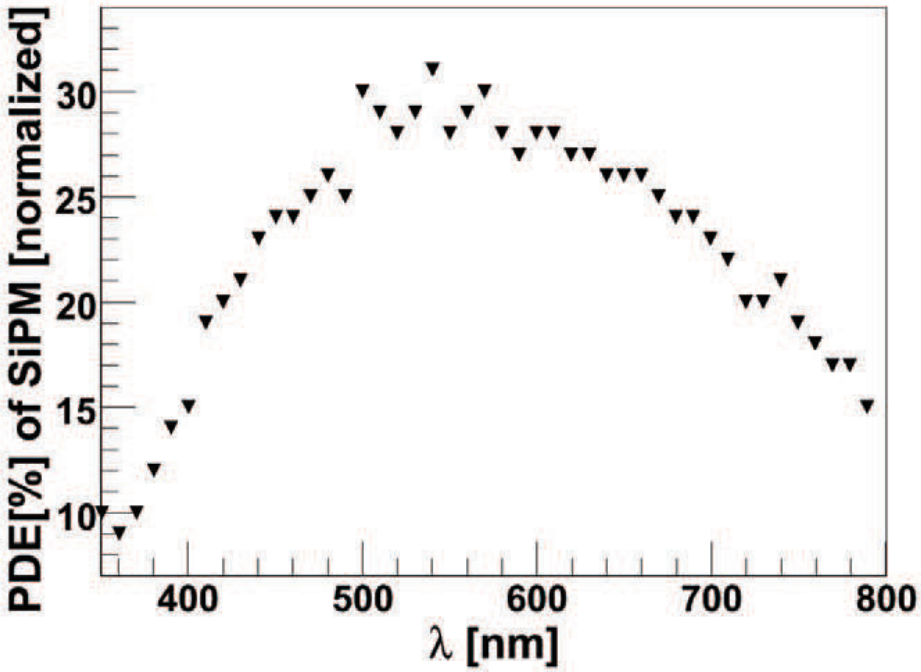

Figure 5.8: Quantum efficiency of a MAPD-3N sample, measured by GSI.

Chapter 6

Conclusion and outlook

The goal of this thesis has been the characterization of the MAPD3-N Geiger-mode APD from Zecotek Photonics. In order to determine as many of the parameters as possible, a great effort has been made in order to increase the signal-to-noise ratio of the system, and to provide an over all better stability and reproducibility of the measurements. One of the most important parameters of a G-APD is its gain, i.e. the intrinsic amplification of the detector. This parameter has been measured successfully for four samples of the MAPD3-N. Ideally a larger set of samples should be tested, in order to have better statistics of the variations from sample to sample. The gain varies to some degree between the individual samples, but lie in the region of 5.4E4 to 6.5E4 while operated at 90 V. Attempts were made to measure the dark rate, as this value is a major cause of noise in the system at low light intensities, but due to limitations in the signal-to-noise ratio this was unfortunately not possible to measure with the current configuration. The signal-to-noise limitations also made attemts of measuring the gain of MAPD3-A samples, the predecessor of the MAPD3-N, unsuccessful. After the development of the MAPD3-N, with its greatly improved performance, the MAPD3-A is not likely to be used for future experiments, and its characterization is mostly interesting in order to test the limitations of the experimental setup.

The gain of the MAPD varies with the temperature, and was found to have a linear decrease of $\sim 2 \cdot 10^3$ per increment of 1° C in temperature of the device. For the optimal bias voltage, this corresponds to a difference of $\sim$4 % per $^\circ$ C, and it is therefore an important parameter to keep in mind when operating the MAPD in an environment where significant fluctuations in the temperature occurs.

The final parameter determined in the thesis was the photon detection efficiency (PDE). This parameter yields information about the spectral response of the device, i.e. how well it performs for various wavelengths of incident light. Knowing this parameter is important when choosing the appropriate wavelength shifter to a scintillator, or choosing a proper wavelength shifting fiber in experiments where the MAPD is used for the readout. Determining this parameter proved to be a challenge, and even though the shape of the Quantum Efficiency (QE) plots obtained yields information about the peak wavelengths, found to be

in the range of $\sim 460 - 600$ nm, the experimental setup still needs to be developed and improved further in order to obtain the absolute values for the QE if the samples.

Having concluded the results of this thesis, it is seen that there is room for improvements of the setup for further characterizing of G-APDs. An issue that will always limit the resolution of the setup, is the noise of the system. Further improvements of the signal-to-noise ratio would provide possibilities for better results, and open up for the characterization of more parameters, such as the dark rate of the MAPD3-N. As for the PDE-measurements there are many systematic errors that can be limited or removed in order to produce better results. Some of these improvements are:

- Refining the framework that aligns the fiberoptical cables with the detectors, placing the fibers at an equally short distance from the sensitive volume for both the PMT and the G-APD. This would limit the uncertainties caused by the dispersion of light.
- Adding a collimator-plate with a small hole in the center, in front of both detectors. If the hole is small enough to ensure that all the light passing through it will hit the sensitive volume, and the hole is of equal size for both devices, the uncertainty related to varying sizes of the sensitive area from detector to detector is limited or removed.
- Changing the position of the detectors with each other after one measurement series, and then performing a second series and average the results, would limit the uncertainty resulting from a potential uneven distribution of light through each of the two ends of the splitted fiberoptical cable.
- Replacing the illumination system in order to provide a more stable, uniform output at a wide range of wavelengths would improve the statistics of the measurements, and remove potential effects caused by an uneven distribution of light throughout the measurement series.

However, a first estimate shows a QE of about 35

Another interesting parameter to look into in the future, is the uniformity of the MAPD pixels. An XY-table able to scan through the pixels of MPPC detectors has been assembled by Andreas T. Samnøy [2]. A few changes are needed to the setup in order to compensate for the lower gain of the MAPD3, compared to the MPPC. Attempts of using the setup was done, but the signal vanished in the noise. However, implementing the new preamplifier used in the experimental setup described in this thesis could provide the improvement needed to the signal-to-noise ratio, and successful measurements may be within reach. The pixels of a MAPD can not be seen by the camera used in the XY-table setup, but it can still scan through the MAPD and illuminate it at steps of a given distance, and in this way investigate the gain for pixels at various locations of the detectors sensitive volume.

Bibliography

[1] H. A. Erdal. Characterization of multipixel avalanche photodiodes. Master's thesis, University of Bergen, Department of physics and technology, 2009.

[2] A.T. Samnøy. Automated xy-table for the characterisation of arrays of pixel sensors for photons and charged particles. Master's thesis, University of Bergen, Department of physics and technology, 2010.

[3] C. Grupen and B. Shwartz. *Particle Detectors*. Cambridge monographs on particle physics, nuclear physics and cosmology. Cambridge University Press, 2nd edition, 2008.

[4] B. Rossi. *High Energy Particles*. Prentice-Hall, 1952.

[5] W.R. Leo. *Techniques for Nuclear and Particle Physics Experiments*. Springer-Verlag, second edition, 1994.

[6] H.A. Bethe & W. Heitler. Stopping of fast particles and creation of electron pairs. *Proc. R. Soc. Lond*, A(146):83–112, 14934.

[7] Particle Data Group. Review of particle properties. *Phys. Lett.*, 239:1–516, 1990.

[8] Particle Data Group. Review of particle properties. *Phys. Rev.*, D(45):1–574, 1992. Phys. Rev. **D46** (1992) 5210-0 (Errata).

[9] Particle Data Group and S. Eidelman et al. Review of particle physics. *Phys. Lett.*, B(592):1–1109, 2004. W.-M. Yao et al., J. Phys. **G33** (2006) 1-1232; http://pdg.lbl.gov.

[10] T.F. Thorsteinsen. Kompendium i strålingsfysikk - fys233. published by the Institute of Physics and Technology, University of Bergen, January 1995.

[11] E.B. Podgoršak. *Radiation Physics for Medical Physicists*, volume Biological and Medical Physics, Biomedical Engineering. Springer-Verlag Berlin Heidelberg, 2006.

[12] K. Kleinknecht. *Detectors for Particle Radiation*. Cambridge Univeristy Press, 2nd edition, 1998.

[13] S.Tavernier. *Experimental Techniques in Nuclear and Particle Physics*. Springer-Verlag, 2010.

[14] R. Nave. Phonons and the debye specific heat. Hyperphysics, july 2010.

[15] P.A. Rodnyi. *Physical processes in inorganic scintillators*. CRC Press, 1997.

[16] R.F. Wallis M.Balkanski. *Semiconductor Physics and Applications*. Oxford University Press, 2000.

[17] R. Nave. Fermi level. Hyperphysics, july 2010.

[18] H. Spieler. *Semiconductor Detector Systems*. Oxford Science Publications, 2005.

[19] S.M. Sze. *Physics of Semiconductor Devices*. Wiley, New York, 2nd edition, 1981.

[20] Hamamatsu Photonics K.K. Photomultiplier tubes, basics and applications. `http://sales.hamamatsu.com/assets/applications/ETD/pmt_handbook_complete.pdf`, February 2006.

[21] G.F. Knoll. *Radiation Detection and Measurement*. Wiley, 3rd edition, 2000.

[22] M. Levinshtein, J. Kostamovaara, and S. Vainshtein. *Breakdown phenomena in semiconductors and semiconductor devices*, volume 36 of *Selected Topics in Electronics and Systems*. World Scientific, 2005.

[23] M.E. Levinshtein, S.L. Rumyantsev, and M.S. Shur. Editors: Handbook series of semiconductor parameters, 1: Elementary semiconductors and a3b5 compounds: Si, ge, c, gaas, gap, gasb, inas, inp, insb. *World Sci. Publ. Co.*, 1996.

[24] Y. Musienko et. al. A simple model of EG&G reverse reach-through APDs. *Nuclear Instruments and Methods in Physics Research A*, A(442):179–186, 2000.

[25] R.J. McIntyre. Multiplication noise in uniform avalanche diodes. *IEEE Transactions on Electron Devices*, ED-13(1):164–168, January 1966.

[26] G. Lutz. *Semiconductor Radiation Detectors*. Springer, 1st edition, 1999.

[27] J.P.R. David and G.J. Rees. The physics of low noise avalanche photodiodes. University of Sheffield, U.K.

[28] B.F.Aull et.al. Geiger-mode avalanche photodiodes for three-dimensional imaging. *Lincoln Laboratory Journal*, 13(2):335–350, 2002.

[29] V.D. Kovaltchouk et. al. Comparison of a silicon photomultiplier to a traditional vacuum photomultiplier. *Nuclear Instruments and Methods in Physics Research*, A(538):408–415, 2005.

[30] D.Renker. New developments on photosensors for particle physics. *Nuclear Instruments and Methods in Physics Research A*, 598:207–212, 2009.

[31] Y. Musienko et. al. Radiation damage studies of multipixel geiger-mode avalanche photodiodes. *Nuclear instruments and methods in Physics Research*, A(581):433–437, 2007.

[32] P. Buzhan et.al. An advanced study of silicon photomultiplier. *ICFA Instrumentation bulletin*, Fall 2001. `http://www.slac.-stanford.edu/pubs/icfa/`.

[33] A.N. Otte et. al. A test of silicon photomultipliers as readout for pet. *Nuclear Instruments and Methods in Nuclear Research*, A(545):705–715, 2005.

[34] N. Otte. The silicon photomultiplier - a new device for high energy physics, astroparticle physics, industrial and medical applications. SNIC Symposium, Stanford, California, April 2006. `http://www.slac.stanford.edu/econf/C0604032/papers/0018.pdf`.

[35] H.-G. Moser. Silicon detector systems in high energy physics. *Progress in Particle and Nuclear Physics*, 63:186–237, 2009.

[36] N. Anfimov. Novel micropixel avalanche photodiodes (mapd) with superhigh pixel density. Presented at the 12th Vienna Conference on Instrumentation, Feb. 15-20, 2010. `http://www1.jinr.ru/Preprints/2010/032%28E13-2010-32%29.pdf`.

[37] B. J. Roy. Geiger apds as possible photon counter for cherenkov detectors. *GSI Scientific Report*, Instruments-Methods(33):313, 2009.

[38] Z. Sadygov et. al. Performance of new micro-pixel avalanche photodiodes form zecotek photonics. *Nuclear Instruments and Methods in Physics Research*, A(610):381–383, 2009.

[39] I. Britvitch. Characterization of geiger-mode avalanche photodiodes for medical imaging applications. *Nuclear Instruments and Methods in Physics Research A*, 571:308–311, 2007.

[40] A. Stoykov et. al. On the limited amplitude resolution of multipixel geiger-mode apds. *Journal of Instrumentation*, 2(6), June 2007.

[41] I. Britvitch and D. Renker. Measurements of the recovery time of geiger-mode avalanche photodiodes. *Nuclear Instruments and Methods in Physics Research*, A(567):260–263, 2006.

[42] A.S. Huntington et. al. Improved breakdown model for estimating dark count rate in avalanche photodiodes with inp and inalas multiplication layers. SPIE Defence and Security Symposium - Pre-release Manuscript 6214-29. `http://www.voxtel-inc.com/whitePapers/SPIE_Voxtel-Inc_6214-29.pdf`.

[43] J.-W. Choe et.al. Resonant tunneling times in superlattice structures. *Journal of Applied Physics*, 79(10):7510–7513, 1996.

[44] NA49 future Collaboration. Study of hadron production in hadron-nucleus and nucleus-nucleus collisions at the cern sps. `http://na49future.web.cern.ch`, November 2006.

[45] M.Golubeva et.al. Longitudinally segmented lead/scintillator hadron calorimeter with micro-pixel apd readout. *Nuclear Instruments and Methods in Physics Research*, A(598):268–269, 2009.

Appendix A

Pre-amplifier gain

The gain measurements for the preamplifier was made by sending a pulse simultaneously to through the preamplifier to a oscilloscope, and directly to the oscilloscope by two cables. A 10 $M\Omega$ resistance was attached in series with one of the connectors of the preamplifier where the MAPD would normally be mounted, and the signal was read out over a 50 Ω resistance at the input of the oscilloscope. The signal from the signal generator was a sine-wave with a frequency of 10 MHz, and the amplitude was varied from 20 mV to 150 mV in steps of 10 mV, in order to observe the gain for various inputs (see Table A.1). The pre-amplifier was found to have a mean current to current amplification of 196.9, with a standard deviation of 0.3 This leads to a current to voltage amplification of $\sim 197 \cdot 50$ as the signal was read out over a 50 Ω resistance. The schematics for the preamplifier can be seen in Figure A.1.

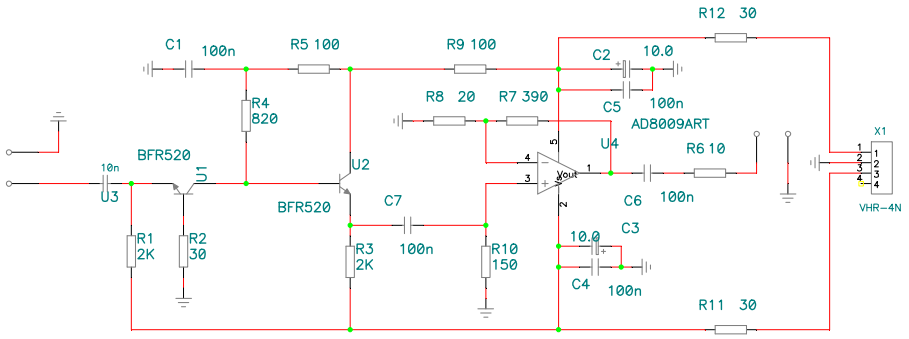

Figure A.1: The schematics for the fast preamplifier, provided by the INR, Moscow.

Table A.1: The gain of the preamplifier from INR

Amplitude [mV]	V_{in} [V]	V_{out}out[V]	I_{in} [A]	I_{out} [A]	Gain
150	0.28	0.27	2.8E-05	0.0055	196.6
140	0.26	0.25	2.6E-05	0.0051	196.6
130	0.24	0.24	2.4E-05	0.0047	196.7
120	0.22	0.22	2.2E-05	0.0044	196.8
110	0.20	0.20	2.0E-05	0.0040	196.8
100	0.19	0.18	1.9E-05	0.0036	196.6
90	0.17	0.16	1.7E-05	0.0033	196.9
80	0.15	0.15	1.5E-05	0.0029	197.3
70	0.13	0.13	1.3E-05	0.0026	196.7
60	0.11	0.11	1.1E-05	0.0022	197.4
50	0.09	0.09	9.3E-06	0.0018	196.8
40	0.07	0.07	7.4E-06	0.0015	197.3
30	0.06	0.05	5.5E-06	0.0011	197.3
20	0.04	0.04	3.7E-06	0.0007	197.3

Appendix B

Hamamatsu PMT, H6780-02

This appendix presents some characteristics of the Hamamatsu H6780-02 PMT. The cathode radiant sensitivity can be seen in B.1.

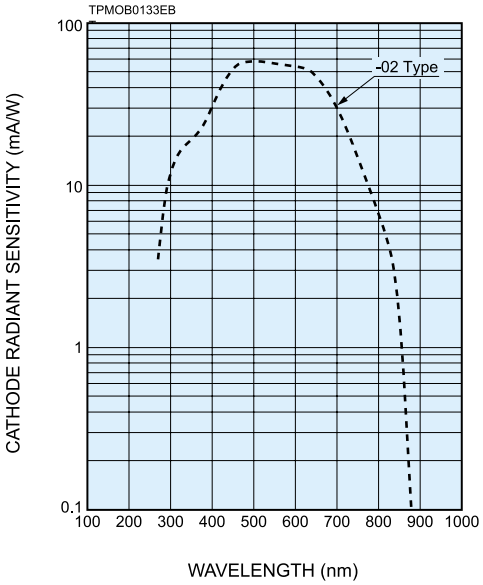

Figure B.1: Cathode radiant sensitivity of the Hamamatsu PMT, H6780-02.